Modeling nonplanar hydraulic fracture propagation using the XFEM: An implicit level-set algorithm and fracture tip asymptotics

Elizaveta Gordeliy [a,*], Safdar Abbas [b], Anthony Peirce [c]

[a] *formerly, Schlumberger-Doll Research Center, Cambridge, MA, USA*
[b] *Schlumberger, Sugar Land, TX, USA*
[c] *Department of Mathematics, University of British Columbia, Vancouver, BC, Canada*

ABSTRACT

We describe the development of a fluid-coupled 2D extended finite element method (XFEM) algorithm to model the propagation of nonplanar radially-symmetric hydraulic fractures. The model determines the fracture propagation trajectory according to the maximum tangential stress criterion of Erdogan and Sih (1963). An implicit level-set algorithm (ILSA) is employed for locating the moving fracture front. The aim of the paper is to validate the radially-symmetric XFEM-ILSA model for nonplanar fracture propagation for mixed modes I and II. First, the results of the model are compared to the analytical solution for viscosity-dominated propagation of a penny-shaped crack. Next, we compare the results of the XFEM-ILSA scheme to the results of laboratory experiments and the results of an axisymmetric displacement discontinuity model for the near-surface propagation of hydraulic fractures with fluid lag (Bunger et al., 2013). For this comparison, a mixed-mode toughness tip asymptote is employed within ILSA to locate the fracture front. An improved algorithm is used for locating the fluid front within the fracture.

© 2018 Elsevier Ltd. All rights reserved.

1. Introduction

One of the current trends and open problems in hydraulic fracture (HF) modeling is the development of 3D models able to capture complex nonplanar fracture geometries. Such models are used, e.g., to model near-wellbore fracture complexity (Sherman et al., 2015; Zhang and Mack, 2016; Cherny et al., 2016), hydraulic fracture propagation in naturally fractured rock (Damjanac et al., 2013; Settgast et al., 2017), and multiple simultaneously propagating fractures that curve due to stress shadow interactions and well interference (Wong et al., 2013; Castonguay et al., 2013; Kumar and Ghassemi, 2016). Development of a numerical model for hydraulic fracture propagation is a challenging task that involves devising a coupling scheme between the deformation of the solid medium, the fluid flow, and a tracking algorithm for the fracture front. The development of an accurate numerical model for this non-linear moving-boundary problem requires proper validation and verification of the resulting numerical solution (Lecampion et al., 2018). Verification of 3D HF models is typically performed for simplified fracture geometries, for which reference solutions exist. Examples are verifications of the numerical solutions against an analytic solution for a planar radially symmetric hydraulic fracture (Searles et al., 2016; Gupta and Duarte, 2016; Settgast et al., 2017), and a comparison of the results of a 3D model with the numerical results for nonplanar 2D fracture reorientation near a wellbore under plane strain conditions (Sherman et al., 2015). A verification for a nonplanar 3D hydraulic fracture can also be performed using the reference solution provided by an axisymmetric nonplanar hydraulic fracture model as done in Sherman et al. (2015) and Fata (2016), in which the results of 3D models were compared to the results of 2D axisymmetric models for bowl-shaped hydraulic fractures.

In this paper, we further develop a 2D plane strain hydraulic fracture model (Gordeliy and Peirce, 2013b), based on the extended finite element method (XFEM), to handle nonplanar axisymmetric hydraulic fractures. The axisymmetric fluid-coupled XFEM simulator provides a verification tool for the development of fully 3D hydraulic fracture models. Despite the fact that it does not include mode-III (tearing) fracture growth, it does provide the first step in the verification of the implementation of fluid flow and nonplanar fracture propagation. In addition, this simulator provides means to study interaction of multiple simultaneously propagating fractures in the absence of stress barriers (Abbas et al., 2016).

The XFEM is based on the finite element method. It represents the discontinuities, including fractures, by augmenting the standard set of finite-element shape functions by enrichment functions in elements around these features (Moës et al., 1999; Stolarska

et al., 2001; Sukumar and Prevost, 2003; Fries and Belytschko, 2010). The underlying finite element mesh does not have to adhere to the geometry of the fractures, and fracture propagation can be modeled in the XFEM without computationally intensive remeshing. Recently, the XFEM has been used for modeling 2D and 3D hydraulic fracture propagation (see Lecampion, 2009; Gordeliy and Peirce, 2013a; Gordeliy and Peirce, 2013b; Weber et al., 2013; Zielonka et al., 2014; Searles et al., 2016; Gupta and Duarte, 2016; Faivre et al., 2016; Haddad and Sepehrnoori, 2016 and references therein, see also Lecampion et al., 2018; Peirce, 2016 for recent reviews). For fracture-front tracking, some of the XFEM HF models have used a propagation criterion based on the fracture toughness (Gordeliy and Peirce, 2013a; 2013b; Weber et al., 2013); other XFEM models have used a cohesive zone approach (e.g., Searles et al., 2016; Faivre et al., 2016; Haddad and Sepehrnoori, 2016).

We consider two limiting regimes of hydraulic fracture propagation in an impermeable medium: the toughness-dominated regime and the viscosity-dominated regime. For a relatively small fluid viscosity and/or injection rate, and a relatively large toughness, the fracture propagates in the toughness-dominated regime, for which the energy spent creating new fracture surface dominates the viscous energy spent driving the fluid through the fracture. For a relatively large fluid viscosity and/or injection rate, and a relatively small toughness, the fracture propagates in the viscosity-dominated regime, for which, conversely, the viscous energy dominates.

The 2D XFEM model, presented in Gordeliy and Peirce (2013b), employed the implicit level-set algorithm (ILSA) (Peirce and Detournay, 2008) to locate the fracture front. The ILSA approach is based on the assumption that the crack width near the crack tip follows a known asymptotic crack-width function (Peirce and Detournay, 2008). Such crack-tip asymptotes have been developed for several regimes of hydraulic fracture propagation (Garagash et al., 2011; Dontsov and Peirce, 2015), for planar fractures and are based on the result (Peirce and Detournay, 2008) that the crack width near the smooth front of a planar fracture reduces to the equations for a one-dimensional (plane strain) semi-infinite crack propagating with a given velocity. Thus, knowledge of the crack width solution near the crack tip makes it possible to predict the extension of the fracture front with time, by inverting the crack-tip asymptote.

We first verify the results of the axisymmetric XFEM-ILSA model against the analytic solution for the viscosity-dominated propagation of a penny-shaped crack (Savitski and Detournay, 2002). The XFEM results show excellent agreement with the analytic solution, even for a relatively coarse finite element mesh.

Next, we apply the ILSA logic to nonplanar fracture propagation in a mixed I-II mode. We employ the toughness tip asymptote to propagate the fracture. For a mode-I fracture, the toughness tip asymptote is obtained by enforcing that the mode-I stress intensity factor is equal to the fracture toughness. For a mixed-mode fracture, the toughness asymptote is obtained using the expression for a mixed-mode stress intensity factor consistent with the propagation criterion of Erdogan and Sih (1963). The resulting mixed-mode tip asymptote relates the combined behavior of the crack width and the shear displacement jump to the fracture toughness K_{Ic} and can be inverted to find the extension of the fracture front.

For validation and verification of the present XFEM-ILSA model for nonplanar fractures, we compare the results of the XFEM-ILSA scheme to the results of laboratory experiments for near-surface propagation of hydraulic fractures with fluid lag (Bunger et al., 2013). The comparison includes verification against the results of an independent axisymmetric model based on the displacement discontinuity method (DDM) (Gordeliy and Detournay, 2011; Bunger et al., 2013). The XFEM model is able to represent the finite specimens in the experiments. By contrast, the DDM model in Bunger et al. (2013) approximated the finite specimens by a half-

space. To locate the fluid front within the fracture, the XFEM model uses an improved algorithm with logic as how to treat artificial negative values of the fluid pressure arising due to numerical overestimation of the fluid front location. The comprehensive comparison of the results from the XFEM with the results from the DDM and with the laboratory data validates the present XFEM model. In addition, it reveals which components of the present model (that are missing in the DDM model, such as a finite specimen size) affect the fracture path and other fracture characteristics.

The present XFEM HF model is a further development of the XFEM-ILSA model (Gordeliy and Peirce, 2013b) to be able to capture nonplanar axisymmetric fractures. Nonplanar fractures are represented using the hybrid explicit-implicit crack description of Fries and Baydoun (Fries and Baydoun, 2012). The main contributions of this work are the development and testing of mixed-mode hydraulic fracture propagation within the ILSA framework, and a detailed validation of the axisymmetric XFEM HF model with laboratory experiments. An improved algorithm is used to treat artificial negative values of fluid pressure within the partially-filled fracture for tracking the fluid front.

2. Problem formulation

2.1. Model of a hydraulic fracture

We consider the propagation of a radially symmetric hydraulic fracture in an impermeable elastic medium characterized by a Young's modulus E, Poisson's ratio ν, and fracture toughness K_{Ic} (see Fig. 1). The fracture is driven by the injection of a Newtonian fluid having a dynamic viscosity μ. The fluid is injected from a wellbore of radius R_w, at a time-varying volumetric rate $Q(t)$. A cylindrical coordinate system (r, z) is introduced such that the z-axis is the axis of radial symmetry. In the (r, z)-plane, the fracture geometry is represented by a 1D curve Σ evolving with time t (Fig. 1b). Along Σ we introduce a curvilinear coordinate s, whose origin $s = 0$ is located at the fracture inlet on the wellbore wall. The fracture length $\ell(t)$ is defined as the arc length of the curve Σ. During fracture propagation, the fluid front may lag behind the fracture front. The location of the fluid front on the curve Σ is denoted as $\ell_f(t)$. The fracture radius at time t is denoted $R(t)$, and the radius of the fluid front is denoted as $R_f(t)$. Note that the fracture radius R and the fluid front radius R_f are the projections of the fracture front and the fluid front onto the plane $z = 0$, respectively (Fig. 1c). With these definitions, the locations on the crack given by $s = 0$, $s = \ell_f$, and $s = \ell$ correspond to $r = R_w$, $r = R_f$, and $r = R$, respectively.

The medium is subject to axisymmetric stresses, applied as tractions at the finite boundaries or as far-field stresses for an infinite domain.

The fracture propagation model determines the fracture curve $\Sigma(t)$, the location of the fluid front $\ell_f(t)$, the fracture width $w(s, t)$, and the fluid pressure $p_f(s, t)$ in the fluid-filled part of the fracture ($s < \ell_f(t)$), all of which evolve with time t.

Throughout the paper, we employ scaled material parameters K', E', and μ', defined by

$$K' = \left(\frac{32}{\pi}\right)^{1/2} K_{Ic}, \quad E' = \frac{E}{1 - \nu^2}, \quad \mu' = 12\mu \tag{1}$$

2.2. Governing equations

2.2.1. Elasticity

The computational domain is denoted by V, and its outer boundary is denoted by Γ. The axisymmetric displacement field $\mathbf{u}$ and the stress field $\boldsymbol{\sigma}$ at a point $\mathbf{x} \in V$ are defined with respect to a cylindrical coordinate system (r, z). The equilibrium equation
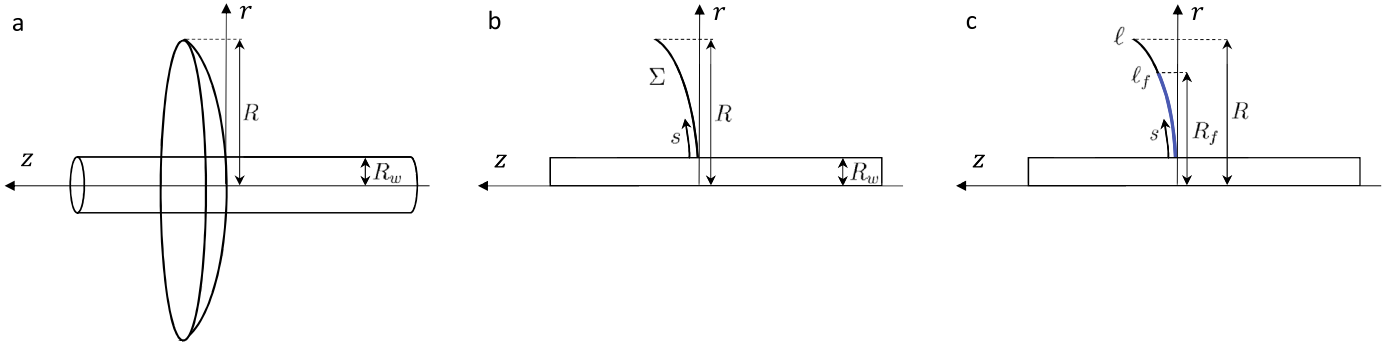
Fig. 1. (a) A nonplanar radially symmetric hydraulic fracture propagating from a wellbore. (b) 2D representation of fracture geometry in cylindrical coordinates. (c) Fracture and fluid fronts: fracture length ℓ, fluid front location ℓ_f, fracture radius R, and fluid front radius R_f. The fluid-filled part of the fracture is shown in blue. (For interpretation of the references to color in this figure legend, the reader is referred to the web version of this article.)
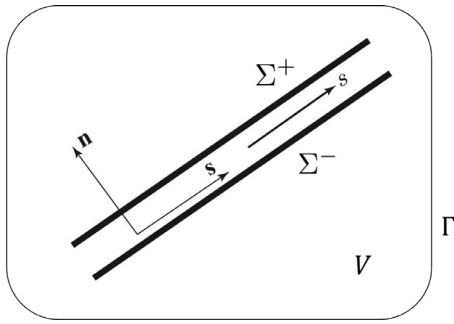
Fig. 2. Orientation of the unit normal vector and the unit tangent vector along the crack and the two crack faces Σ^+ and Σ^-. Adapted from Gordeliy and Peirce (2015).

and Hooke's law for the linear elastic medium can be written in the following form:

$$\nabla \cdot \boldsymbol{\sigma} = \mathbf{0} \tag{2}$$

$$\boldsymbol{\sigma} = \mathcal{C} : \boldsymbol{\varepsilon}(\mathbf{u}) \tag{3}$$

in which $\mathcal{C}$ is the tensor of elastic constants, and $\boldsymbol{\varepsilon}(\mathbf{u})$ is the strain tensor associated with the displacement $\mathbf{u}$,

$$\boldsymbol{\varepsilon}(\mathbf{u}) = \frac{1}{2}\left(\nabla\mathbf{u} + (\nabla\mathbf{u})^T\right) \tag{4}$$

The unit normal and the unit tangent vectors along the crack are denoted by $\mathbf{n}$ and $\mathbf{s}$, respectively (Fig. 2). At each point $s \in \Sigma$, the unit tangent vector $\mathbf{s}$ is tangent to the crack and oriented in the direction of increasing coordinate s, and the unit normal vector $\mathbf{n}$ is oriented in a direction rotated $\pi/2$ counterclockwise from $\mathbf{s}$. The two crack faces are identified as Σ^+ and Σ^-, such that the normal vector $\mathbf{n}$ points in the direction from Σ^- to Σ^+. The values of the displacement and the stress along each face are denoted by $\mathbf{u}^+$ and $\mathbf{u}^-$ and by $\boldsymbol{\sigma}^+$ and $\boldsymbol{\sigma}^-$, respectively.

The normal and the tangential displacement jumps across the crack define, respectively, the crack width w and the ride v:

$$w = [[\mathbf{u}]]_\Sigma \cdot \mathbf{n} = (\mathbf{u}^+ - \mathbf{u}^-) \cdot \mathbf{n} \tag{5}$$

$$v = [[\mathbf{u}]]_\Sigma \cdot \mathbf{s} = (\mathbf{u}^+ - \mathbf{u}^-) \cdot \mathbf{s} \tag{6}$$

The normal and the shear tractions on the crack are obtained from the stress tensor as $\sigma_n^\pm = \mathbf{n}^T(\boldsymbol{\sigma}^\pm \cdot \mathbf{n})$ and $\sigma_s^\pm = \mathbf{s}^T(\boldsymbol{\sigma}^\pm \cdot \mathbf{n})$.

The specific boundary conditions on the outer boundary Γ are described in Section 5 for each modeling example. For each point $\boldsymbol{x} \in \Gamma$, either a zero displacement $u_i(\boldsymbol{x}) = 0$ or a given boundary traction $t_i(\boldsymbol{x}) = t_i^*(\boldsymbol{x})$ is prescribed, in each coordinate direction ($i = r, z$). We denote those parts of Γ with prescribed displacement components, $u_i(\boldsymbol{x}) = 0$, as $\Gamma_{u,i}$, and those parts of Γ with prescribed traction components, $t_i(\boldsymbol{x}) = t_i^*(\boldsymbol{x})$, as $\Gamma_{t,i}$.

In the particular case, for which the domain V is infinite and subjected to nonzero far-field stresses σ_{ij}^∞, the problem is reduced to the problem of an infinite domain with zero displacements at infinite boundaries, as follows. The problem is decomposed into a superposition of problems (a) with the loaded crack and zero far-field stress and (b) without the crack and with nonzero applied far-field stresses σ_{ij}^∞ (for which the complete stress field $\boldsymbol{\sigma}^{\infty,b}$ is known in the domain V). The traction vector on the crack in problem (a) is modified using superposition by adding the following applied stresses along the crack:

$$\sigma_n^\infty = -\mathbf{n}^T\boldsymbol{\sigma}^{\infty,b}\mathbf{n}, \quad \sigma_s^\infty = -\mathbf{s}^T\boldsymbol{\sigma}^{\infty,b}\mathbf{n} \tag{7}$$

Additionally, we assume that the problem (a) with zero far-field stresses is equivalent to the problem with zero far-field displacement. Therefore, the problem of an infinite domain V with nonzero far-field stress is reduced to the problem of an infinite domain with a vanishing displacement at infinity.

The normal traction σ_n on the crack is equal to the fluid pressure (but opposite in sign) within the fluid-filled portion of the crack and is equal to zero in the fluid lag zone; the shear traction σ_s is assumed to be zero everywhere along the crack surface. Additionally, for an infinite domain V with nonzero far-field stress, the stresses (7) induced by the far-field stresses are applied along the crack. These boundary conditions on the fracture are formulated as follows:

$$\sigma_n^+ = \sigma_n^- = -p_f + \sigma_n^\infty, \quad 0 < s < \ell_f \tag{8}$$

$$\sigma_n^+ = \sigma_n^- = \sigma_n^\infty, \quad s \geq \ell_f \tag{9}$$

$$\sigma_s^+ = \sigma_s^- = \sigma_s^\infty, \quad 0 < s < \ell \tag{10}$$

For a finite domain, $\sigma_n^\infty = \sigma_s^\infty = 0$, and the superposition principle is not applied.

In our previous work (Gordeliy and Peirce, 2013a; 2013b; 2015), we discussed two boundary value problems for the elastic deformation of a medium with a crack that need to be solved repeatedly during the modeling of a propagating HF:

(I) $P \rightarrow W$ (Neumann to Dirichlet map): Given the Neumann boundary conditions (8)–(10) along the crack, with prescribed fluid pressure p_f, determine the crack width w along the crack Σ.

(II) *P&W* (Mixed): Given the asymptotic crack width function w_{tip} in a neighbourhood Σ_t of the crack tip,

$$w(s) = w_{tip}(s), \quad s \in \Sigma_t \tag{11}$$

and the prescribed fluid pressure p_c in the interior of the crack (channel) $\Sigma_c = \Sigma \setminus \Sigma_t$,

$$p_f(s) = p_c(s), \quad s \in \Sigma_c \tag{12}$$

determine the crack width w within the channel Σ_c. Thus in the *P&W* scheme, the boundary conditions in the channel Σ_c are (8)–(10), with the given fluid pressure $p_f = p_c$. In the tip region Σ_t, the boundary conditions are (10) and (11), with a prescribed crack-tip asymptote w_{tip}.

The $P \rightarrow W$ formulation is used in the present paper for the problem of a hydraulic fracture with fluid lag. The *P&W* formulation is advantageous for the case when there is no fluid lag and the fluid pressure near the crack front is characterized by singular behavior (see Detournay and Peirce, 2014). The use of the crack-tip asymptote for the crack width makes it possible to avoid having to represent such a singular pressure numerically. The *P&W* formulation is used in the present paper for the problem of a hydraulic fracture without fluid lag propagating in the viscosity-dominated regime.

2.2.2. Fluid flow

We assume that lubrication theory is applicable to the problem of interest. The fluid flow equations are formulated for the fluid-filled portion of an axisymmetric fracture, defined by $0 < s < \ell_f(t)$. For the case when there is no fluid lag, $\ell_f = \ell$.

The conservation of mass can be expressed as

$$\frac{\partial w}{\partial t} + \frac{1}{r} \frac{\partial (rq)}{\partial s} = 0, \quad 0 < s < \ell_f(t) \tag{13}$$

where $q(s, t)$ is the fluid flux, related to the pressure gradient via Poiseuille's law:

$$q = -\frac{w^3}{\mu'} \frac{\partial p_f}{\partial s}, \quad 0 < s < \ell_f(t) \tag{14}$$

The boundary condition for the fluid flux at the fracture inlet on the wellbore wall is expressed via the injection rate $Q(t)$, which can be time dependent and has units of [volume/time]:

$$\lim_{r \to R_w} (2\pi r q) = Q(t) \tag{15}$$

The fluid front does not necessarily coincide with the fracture front. If the fluid front lags behind the fracture front, there are two boundary conditions on the fluid front (Detournay and Peirce, 2014): a zero fluid pressure at the fluid front

$$p_f = 0, \quad s = \ell_f(t) \tag{16}$$

and the Stefan condition for the fluid front velocity, $\dot{\ell}_f(t)$

$$\dot{\ell}_f(t) = \frac{q(\ell_f(t), t)}{w(\ell_f(t), t)} \tag{17}$$

The location of the fluid front at each time instant can be determined from the fluid front velocity (17).

If the fluid and fracture fronts coincide, the Stefan condition (17) is reduced to a zero flux boundary condition:

$$q = 0, \quad s = \ell(t) \tag{18}$$

By integrating the equation of mass conservation (13) over the crack surface and over the time interval since the start of fluid injection at $t = 0$, and using the boundary conditions (15) and (17) (for fluid lag) or (18) (when there is no fluid lag), one can obtain the global fluid volume balance equation

$$\int_0^{\ell_f(t)} 2\pi r w(s, t)\, ds = \int_0^{\ell_f(0)} 2\pi r w(s, 0)\, ds + \int_0^t Q(t')\, dt' \tag{19}$$

where $\ell_f(0)$ and $w(s, 0)$ denote, respectively, the location of the fluid front and the crack width at time $t = 0$.

2.2.3. Propagation criterion and tip asymptotics

The moving fracture front $\ell(t)$ is determined from a fracture propagation criterion. Following previous work (Peirce and Detournay, 2008; Gordeliy and Peirce, 2013b), we formulate the fracture propagation condition in terms of an asymptotic solution for the fracture width at the fracture front. The fracture propagates in mobile equilibrium and at every instant the fracture width satisfies the fracture tip asymptote. We consider the following two tip asymptotes:

(i) The toughness tip asymptote for a mode I fracture consistent with the condition that the mode I stress intensity factor is equal to the fracture toughness (Rice, 1968a):

$$w \sim \frac{K'}{E'} \hat{s}^{1/2}, \quad \hat{s} \to 0 \quad \text{(mode I)} \tag{20}$$

where $\hat{s} = (\ell - s)$ is the distance from the fracture tip. For the mixed-mode fracture propagation (modes I and II), the corresponding asymptotic condition was formulated in Bunger et al. (2013) by using the propagation criterion of Erdogan and Sih (1963):

$$\cos \frac{\hat{\theta}}{2} \left(w \cos^2 \frac{\hat{\theta}}{2} - \frac{3}{2} v \sin \hat{\theta} \right) \sim \frac{K'}{E'} \hat{s}^{1/2}, \quad \hat{s} \to 0 \quad \text{(modes I and II)} \tag{21}$$

where $\hat{\theta}$ is the angle that maximizes the hoop stress $\sigma_{\theta\theta}$ ahead of the crack. $\hat{\theta}$ is the angle of deflection of the new crack direction with respect to the existing crack-tip orientation. It can be determined in terms of the ratio η of mode II to mode I stress intensity factors:

$$\hat{\theta} = 2 \arctan \left(\frac{1 \pm \sqrt{1 + 8\eta^2}}{4\eta} \right), \quad \eta = \frac{K_{II}}{K_I} = \lim_{\hat{s} \to 0} \frac{v}{w} \tag{22}$$

where w is the crack width, and v is the tangential displacement jump defined in Eq. (6). The sign in the expression (22) for $\hat{\theta}$ is chosen such as to maximize the hoop stress ahead of the crack, which is performed numerically by choosing the sign corresponding to the larger value of the left-hand side expression in Eq. (21).

The toughness tip asymptote is applicable when the energy dissipated by driving the fluid through the fracture is subdominant to the energy required to break the rock (toughness-dominated regime). It is also applicable when the fluid lag is significant so that the tip region of the fracture is not fluid-filled.

(ii) The viscous tip asymptote, applicable for viscosity-dominated fracture propagation without fluid lag, is expressed by the following 2/3 power-law behavior (Desroches et al., 1994),

$$w \sim w_{tip}(s) = \beta_m \left(\frac{\mu'}{E'} \dot{\ell}(t) \right)^{1/3} \hat{s}^{2/3}, \quad \hat{s} \to 0, \quad \beta_m = 2^{1/3} 3^{5/6} \tag{23}$$

where $\dot{\ell}$ is the crack front velocity.

The asymptotic solution, which provides a transition between these two limiting asymptotes, has been developed for a planar (mode I) fracture (Garagash and Detournay, 2000). However, it is based on the assumption that in the toughness-dominated regime, the mode-I stress intensity factor is equal to the fracture toughness, and therefore it is not directly applicable to a mixed-mode fracture propagation.

3. XFEM formulation for elastic deformation of a medium

The formulation of the XFEM for the elastic deformation of the medium with a fracture is based on the previous work for planar fractures (Gordeliy and Peirce, 2013b; 2015). The nonplanar cracks are represented using the hybrid explicit-implicit crack description of Fries and Baydoun (2012). Below, we summarize the XFEM model for completeness.

The XFEM weak formulations, corresponding to the $P \to W$ and to the $P\&W$ boundary-value problems, are discussed in Appendix A. In the $P \to W$ scheme, the fluid pressure is given in the crack as the boundary condition, and the unknowns of the problem are the displacements in the domain. In the $P\&W$ scheme, the crack width is given in the tip region Σ_t by the tip asymptote $w_{tip}(s)$, and the fluid pressure is given in the channel Σ_c. In the $P\&W$ scheme, the unknowns are the displacements in the domain and the components of the stress tensor in the finite elements that overlap with the tip region Σ_t. Once the unknown displacement and stress fields are represented by linear combinations of shape functions, the weak formulation is reduced to a linear system for the displacement degrees of freedom (and stress degrees of freedom, for the $P\&W$ scheme), as in the standard finite element method.

3.1. Shape functions

In the XFEM, interfaces and cracks are represented by augmenting the standard set of Lagrange shape functions by specialized enrichment functions in the elements around these features (Moës et al., 1999; Stolarska et al., 2001; Sukumar and Prevost, 2003; Fries and Belytschko, 2010). Following Gordeliy and Peirce (2013b, 2015), we consider two enrichment schemes: the XFEM-t scheme with crack-tip enrichment, in which cracks are represented by combining a discontinuous sign enrichment and a singular crack-tip enrichment, and the XFEM-s scheme without crack-tip enrichment, in which cracks are represented by a discontinuous sign enrichment only. Sign enrichment defines the geometry of the crack whereas the crack-tip enrichment is required to restore the order of convergence expected of the underlying finite element discretization of the elasticity problem, which degrades due to the presence of the singular behavior at the crack tips. Sign enrichment is relatively inexpensive compared to crack-tip enrichment, which requires computationally intensive spatial integration of the singular enrichment functions in the tip-enriched elements.

The discontinuous sign enrichment and the singular crack-tip enrichment are defined below:

(I) Sign enrichment: elements that intersect the crack are enriched by the sign function $\mathbf{sg}(\mathbf{x})$:

$$\mathbf{sg}(\mathbf{x}) = \text{sign}(\phi(\mathbf{x})), \quad \mathbf{x} \in V \tag{24}$$

$$\phi(\mathbf{x}) = \pm \min_{\tilde{\mathbf{x}} \in \Sigma} |\mathbf{x} - \tilde{\mathbf{x}}| \tag{25}$$

in which $\phi(\mathbf{x})$ is the signed distance function that has different signs on the two sides of the crack.

(II) Crack-tip enrichment: the singular behavior of the displacement at the crack tip is captured by power-law enrichment basis functions (Gordeliy and Peirce, 2015) consistent with the asymptotic behavior of the crack width near the fracture tip, $w_{tip} \sim \hat{s}^\lambda$ with $\frac{1}{2} \leq \lambda < 1$. This range of asymptotes includes the limiting toughness-dominated ($\lambda = \frac{1}{2}$) and viscosity-dominated ($\lambda = \frac{2}{3}$) regimes. The crack-tip enrichment for the displacement comprises the following four singular functions $\{\psi_j^{\mathbf{u}}\}$:

$$\boldsymbol{\psi}^{\mathbf{u},\lambda} = \rho^\lambda \{\sin(\lambda\theta), \cos(\lambda\theta), \sin(\lambda - 2)\theta, \cos(\lambda - 2)\theta\} \tag{26}$$

Here (ρ, θ) are polar coordinates centered at the fracture tip, so that ρ denotes the distance from the fracture tip, and the values $\theta = \pm \pi$ correspond to the two crack faces.

The computational domain V is discretized into quadrilateral elements. In the XFEM-t scheme, the displacement is approximated by functions in the trial space $\mathscr{U}_{\mathbf{u}}^h$,

$$\mathscr{U}_{\mathbf{u}}^h = \left\{ \mathbf{u}^h \mid \mathbf{u}^h \in U, \ u_i^h = 0 \text{ on } \Gamma_{u,i}, \ i = 1, 2 \right\},$$

where the shape function space U is spanned by the following approximations of the displacement components u_k ($k = 1, 2$) :

$$u_k^h = \sum_{i \in I} a_i^k N_i(\mathbf{x}) + R_s(\mathbf{x}) \sum_{i \in I_s^*} b_i^k N_i(\mathbf{x})(\mathbf{sg}(\mathbf{x}) - \mathbf{sg}(\mathbf{x}_i))$$

$$+ R_t(\mathbf{x}) \sum_{i \in I_t^*} N_i(\mathbf{x}) \sum_{j=1}^4 c_i^{j,k}(\psi_j^{\mathbf{u}}(\mathbf{x}) - \psi_j^{\mathbf{u}}(\mathbf{x}_i)) \tag{27}$$

In (27), $\mathbf{x} \in V \backslash \Sigma$; N_i are the standard piecewise bilinear Lagrange basis functions and $a_i^k, b_i^k, c_i^{j,k} \in \mathbb{R}$. The set I_t is the set of all nodes that are within a prescribed radius ρ_t of the crack tip. The set I_s comprises all the nodes of the elements cut by the crack, excluding the nodes already in I_t, so that $I_t \cap I_s = \varnothing$. The set I_s^* is the set of all nodes of elements that are cut by the crack and that have at least one node in I_s, and I_t^* is the set of all nodes in elements that have at least one node in I_t. To prevent the loss of partition of unity in the intermediate elements that have both tip-enriched and non-tip-enriched nodes, the two ramp functions $R_t(\mathbf{x}) = \sum_{i \in I_t} N_i(\mathbf{x})$ and $R_s(\mathbf{x}) = \sum_{i \in I_s} N_i(\mathbf{x})$ are introduced to blend the two enrichments (Fries, 2008). For details, the reader is referred to Gordeliy and Peirce (2015).

In the XFEM-s scheme, cracks are represented by the sign enrichment only, and the crack tip enrichment is not involved. The crack is extended virtually beyond each crack tip, in the direction tangential to the crack, to the farthest edge of the encompassing finite element. The nodal set I_s for the sign enrichment is defined as the set of all nodes of the elements cut by the crack, excluding the two nodes on the farthest edge of that encompassing finite element. The set I_s^* comprises all the nodes of the elements cut by the crack. The approximation space for the displacement is spanned by the shape functions given by Eq. (27), where $I_t^* = I_t = \varnothing$ and $R_t(\mathbf{x}) = 0$. The surface integrals over the crack surface in the crack-tip elements are treated in such a way that there is no contribution to the weak form from integrals over the extended crack surface beyond the actual crack tip. In other words, the crack tip asymptote is imposed in a weak sense. While the sign enrichment does not capture the exact location of the crack tip or the singular behavior of the elastic fields at the crack tips, it is relatively inexpensive compared to the crack-tip enrichment (Gordeliy and Peirce, 2013b; 2015). For the XFEM-s scheme, the sign enrichment only needs to be updated when the fracture front breaks into a new finite element. By contrast, for the XFEM-t scheme the singular crack tip enrichment and the stiffness matrix of the XFEM are updated each time the fracture front is moved.

Further details of the shape functions for the XFEM-t and the XFEM-s schemes, including the enrichment for the stress required in the $P\&W$ scheme, are given in Gordeliy and Peirce (2015).

3.2. Level-set representation of the fracture

To represent a nonplanar crack in the XFEM setting, we use the hybrid explicit-implicit crack description of Fries and Baydoun (2012). The crack is represented by three level-set functions. In the numerical implementation, these level-set functions are employed to determine which nodes of the mesh are to be enriched with either sign or crack-tip enrichments, and to define the curvilinear polar coordinates, $(\rho(\mathbf{x}), \theta(\mathbf{x}))$, associated with the crack and employed in Eq. (26) to calculate the crack-tip enrichment functions. We summarize this approach in Appendix A.3; for further details the reader is referred to Fries and Baydoun (2012).

The advantages of this representation include the ability to explicitly update the crack geometry upon crack propagation, the availability of the level-set representation of the crack to define which nodes of the FEM mesh are to be enriched, the ability to construct the power-law XFEM enrichment (26) in a curvilinear

coordinate system corresponding to the nonplanar crack, and a straight-forward extension from 2D to 3D problems.

3.3. Modeling infinite domains

To model an infinite domain, we employ mapped infinite elements that make it possible to capture a decaying far-field displacement (Zienkiewicz et al., 1983; Marques and Owen, 1984; Bettess, 1992; Zienkiewicz et al., 2013). To represent an infinite domain, assuming a vanishing displacement at infinity, we distribute infinite elements along the boundaries of a finite computational subdomain that includes the crack. Mapping for the infinite elements is performed using the formulation from Zienkiewicz et al. (2013) and Liu and Quek (2003). This formulation makes it possible to use 2D infinite elements that extend to infinity in one direction and are finite in the other direction. The shape functions in the mapped infinite elements are formulated in terms of Lagrange polynomials, as described in our previous work (Gordeliy and Peirce, 2013a) for the singly infinite elements. In the XFEM simulations in Section 5.1, the shape functions in the infinite elements were products of a Lagrange polynomial of order 6 in the infinite direction and a Lagrange polynomial of order 1 (linear) in the finite direction.

4. XFEM-ILSA algorithm for nonplanar fracture propagation

4.1. Hydraulic fracture with fluid lag, P → W XFEM-t scheme

The XFEM-ILSA algorithm was developed in Gordeliy and Peirce (2013b) for planar plane strain fractures without fluid lag. The modifications developed in this paper to model nonplanar fractures with fluid lag are described below. In contrast to Gordeliy and Peirce (2013a), in which the propagation of a nonplanar plane strain fracture with fluid lag was considered, the present work employs the ILSA algorithm for locating the fracture front and an improved algorithm for locating the fluid front with time; in addition, a 1D finite volume scheme replaces the 1D finite-element solution used in Gordeliy and Peirce (2013a) for solving the lubrication equation within the fracture. We use the XFEM to solve for the elastic deformation of the medium containing the propagating HF, and a finite volume scheme to solve for the fluid flow within the HF.

4.1.1. XFEM Solution

For the problem involving a fluid lag, we employ the $P \to W$ XFEM-t scheme in the present work. The curved crack is approximated by multiple line segments, with kinks at finite element edges (Fig. 3). We assume that the crack does not cut through the nodes of the finite element mesh, consistent with the definition of the displacement shape functions that are assumed to be continuous at the nodes (see Appendix D in this regard). We also assume that the crack does not intersect itself.

The crack, cutting N finite elements, is discretized into N straight-line segments comprising the intersections of the crack with the finite elements and referred to as "crack elements". The arc-length coordinate s, equal to the distance from the wellbore along the crack, defines points on the crack. The crack elements are denoted by $[s_i, s_{i+1}]$, where $i = 1, \ldots, N$ and where s_i is equal to the arc-length coordinate of node i. The nodes s_i for $i = 1, \ldots, N$ are located at the finite element edges, and the node s_{N+1} is located at the crack tip. The node $s_1 = 0$ is located at the wellbore wall. The radial coordinate of node s_i is denoted r_i, for all i.

For a problem with fluid lag, where $\ell_f < \ell$, we denote the number of fluid-filled elements by m, and denote the element containing the fluid front (the "partially filled" element) as element $m + 1$,
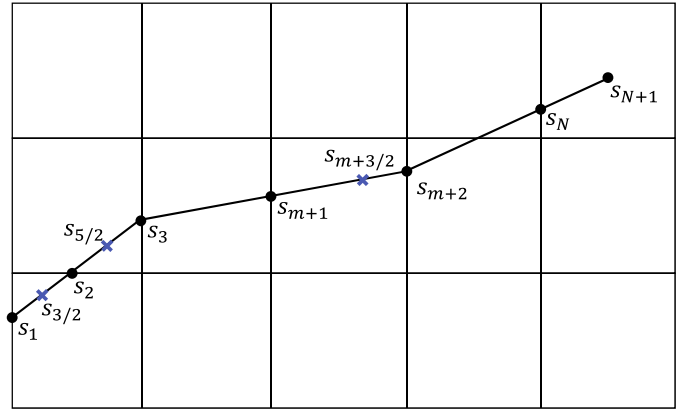

Fig. 3. Discretization of a curved crack with fluid lag within a finite element mesh. Blue crosses denote the pressure nodes $s_{i+1/2}$ for $i = 1, \ldots, m + 1$, where the node $s_{m+3/2} = \ell_f$ corresponds to the location of the fluid front.

such that $s_{m+1} \le \ell_f < s_{m+2}$. To discretize the lubrication equation, we introduce the pressure nodes $s_{i+1/2}$ as follows (Fig. 3):

$$s_{i+1/2} = \frac{s_i + s_{i+1}}{2}, \text{ for } i = 1, \ldots, m \tag{28}$$

$$s_{m+3/2} = \ell_f \tag{29}$$

The approximation of the fluid pressure $p_f(s, t)$ for $s \le \ell_f$ is constructed in terms of piecewise linear basis functions $h_{i+1/2}(s)$ associated with the nodal values $p_{i+1/2} = p_f(s_{i+1/2}, t)$ as follows:

$$p_f(s, t) \approx \sum_{i=1}^{m+1} p_{i+1/2} h_{i+1/2}(s) \tag{30}$$

Functions $h_{i+1/2}(s)$ are defined in Appendix B. Eq. (30) provides a C^0-continuous approximation of p_f in the fluid-filled portion of the crack ($s \le \ell_f$), and ensures that $p_f = 0$ for $s > \ell_f$. Using the linearity of the elasticity problem, and given the nodal pressures $p_{j+1/2}$ ($j = 1, \ldots, m + 1$), the XFEM approximation for the nodal crack widths, $w_i = w(s_i, t)$, is obtained in the form

$$w_i = \sum_{j=1}^{m+1} D_{ij} p_{j+1/2} + \omega_{\sigma,i}, \quad i = 1, \ldots, N \tag{31}$$

In (31), D_{ij} and $\omega_{\sigma, i}$ express, correspondingly, the effects of the pressure basis functions $h_{j+1/2}(s)$ and of the tractions applied to external boundaries of V onto the crack width at node s_i (Appendix B).

4.1.2. Discretization of the fluid flow equations

We denote by m_0 the number of fluid-filled elements at the previous time step $t_0 = t - \Delta t$. We assume that $\dot{\ell}_f \ge 0$, thus $m \ge m_0$. (A formulation for a more general case, when $\dot{\ell}_f$ can become negative, can be obtained in a similar way.) In the following, the superscript "o" denotes the quantities obtained at the previous time step, e.g., $w^o = w(s, t_0)$ and $\ell_f^o = \ell_f(t_0)$ represent, correspondingly, the values of the crack width and of the fluid front at the previous time step t_0.

The volume of fluid in the element $[s_k, s_{k+1}]$ at time t is found from

$$\text{Vol}_f(s_k, s_{k+1}, t) = 2\pi \int_{s_k}^{\min(\ell_f, s_{k+1})} r w \, ds \tag{32}$$

The integrals in Eq. (32) are approximated using the trapezoidal rule. Therefore the approximated volume of fluid in the element

$[s_k, s_{k+1}]$ at time t, denoted Vol_k, is computed for $k = 1, \ldots, m+1$ as follows:

$$\text{Vol}_k = 2\pi \times \begin{cases} \dfrac{r_k w_k + r_{k+1} w_{k+1}}{2}(s_{k+1} - s_k), & k \leq m \\ \dfrac{r_k w_k + R_f w(\ell_f, t)}{2}(\ell_f - s_k), & k = m+1 \end{cases} \quad (33)$$

Similarly, the volume of fluid in the element $[s_k, s_{k+1}]$ at time t_0, denoted Vol_k^o, can be found from Eq. (33) in which w, ℓ_f, and t are replaced, correspondingly, by w^o, ℓ_f^o, and t_0.

By integrating Eq. (13) over the time step Δt and over the element $[s_k, s_{k+1}]$, using the boundary condition (15) at the wellbore inlet and using central differencing for the fluxes in Eq. (14), we obtain the following finite-volume discretization of the fluid-flow equations for elements $[s_k, s_{k+1}]$, for $1 \leq k \leq m-1$:

$$\left[\text{Vol}_k - \text{Vol}_k^o\right] + 2\pi \Delta t (r_{k+1} q_{k+1} - r_k q_k) = 0, \quad 1 \leq k \leq m-1 \quad (34)$$

where

$$r_1 q_1 = \frac{Q(t)}{2\pi} \quad (35)$$

and

$$r_k q_k = -r_k \frac{w_k^3}{\mu'} \frac{p_{k+1/2} - p_{k-1/2}}{s_{k+1/2} - s_{k-1/2}}, \quad k = 2, \ldots, m \quad (36)$$

Note that (34) is a backward Euler approximation to the evolution equation (13). Similarly, by combining the elements $[s_m, s_{m+1}]$ and $[s_{m+1}, s_{m+2}]$, one can obtain the following discretized equation:

$$\left[\text{Vol}_m - \text{Vol}_m^o\right] + \left[\text{Vol}_{m+1} - \text{Vol}_{m+1}^o\right] = 2\pi \Delta t \, r_m q_m \quad (37)$$

The fluid pressure at the fluid front is set to zero:

$$p_f(\ell_f, t) = p_{m+3/2} = 0. \quad (38)$$

4.1.3. Iterative solution of coupled equations

For a given trial crack front ℓ and a trial fluid front ℓ_f at time t, the algorithm determines the N-vector of nodal crack widths $\mathbf{w} = (w_1, \ldots, w_N)$ and the $(m+1)$-vector of nodal fluid pressures $\mathbf{p} = (p_{3/2}, \ldots, p_{m+3/2})$. The elasticity equation (31) is used to express the nodal crack widths in terms of the nodal pressures and to reformulate the nonlinear Reynolds equations (34) and (37) in terms of the nodal pressures $\mathbf{p} = (p_{3/2}, \ldots, p_{m+3/2})$ only. The system of $(m+1)$ nonlinear equations (34), (37), and (38) is solved for the nodal pressures $\mathbf{p} = (p_{3/2}, \ldots, p_{m+3/2})$ using Newton iteration.

4.1.4. Fluid front

The fluid front ℓ_f can be located by using the fluid front velocity $\dot{\ell}_f$:

$$\ell_f = \ell_f^o + \dot{\ell}_f \Delta t \quad (39)$$

The fluid front velocity can be obtained from the Stefan equation (17) and Poiseuille's law (14):

$$\dot{\ell}_f = -\frac{w(\ell_f)^2}{\mu'} \frac{\partial p_f(s)}{\partial s}\Big|_{s=\ell_f^-} \quad (40)$$

where we have omitted the time variable t to keep expressions concise.

For a given location of the crack front ℓ at time t, the present numerical algorithm starts to locate the fluid front ℓ_f by using Eqs. (39) and (40) iteratively: initially the velocity of the fluid front is set to the value at the previous time step, $\dot{\ell}_f^{(1)} = \dot{\ell}_f^o$; at subsequent iterations, the velocity of the fluid front is updated from Eq. (40), and the location of the fluid front is updated from Eq. (39). However, it was found that this iterative procedure may not converge once the fluid front location ℓ_f is overestimated, such

as in case of a relatively rapidly changing injection rate $Q(t)$ in the test case representing the conditions that prevail for the laboratory experiments in Section 5. Indeed, if the overestimation of the fluid front location ℓ_f is too large, the solution of the discretized lubrication equation may lead to a negative fluid pressure $p_f(s) < 0$ near the fluid front, at $s < \ell_f$ and $s \to \ell_f^-$. It was found that, with the negative fluid pressure near the fluid front in the presence of the fluid lag, Eq. (40) does not provide an accurate estimate of the fluid front velocity. Indeed, if the fluid front is advancing (i.e., $\dot{\ell}_f > 0$), Eq. (40) requires a positive pressure gradient at the fluid front (i.e., $\nabla p_f(s)|_{s=\ell_f^-} > 0$), which together with the zero fluid pressure at the fluid front (Eq. (16)), requires that $p_f(s) > 0$ near the fluid front at $s < \ell_f$ and $s \to \ell_f^-$. In other words, a negative fluid pressure near the fluid front (when the fluid lag is non-negligible) violates Eq. (16) and cannot be assumed to provide an accurate solution for the fluid front velocity.

To circumvent the lack of convergence of the iterative fluid front location once a negative fluid pressure has been obtained near the fluid front, in subsequent iterations we solve Eqs. (39) and (40) by finding the root, $\ell_f = \ell_f^*$, of the following function f:

$$f(\ell_f) = \begin{cases} \dfrac{w(\ell_f)^2}{\mu'}\left(\dfrac{\partial p_f(s)}{\partial s}\Big|_{s=\ell_f^-}\right) - \dfrac{\ell_f - \ell_f^o}{\Delta t} & , \; p_f(s) > 0 \text{ for all } s < \ell_f \\ -1 & , \; p_f(s) < 0 \text{ for some } s < \ell_f \end{cases} \quad (41)$$

such that

$$f(\ell_f^*) = 0 \quad (42)$$

The root of the function (41) is found using a bi-section algorithm.

In summary, for a given trial location of the crack front ℓ at time t, the algorithm locates the fluid front ℓ_f by using Eqs. (39) and (40) iteratively and by switching to solving Eq. (42) once a negative fluid pressure has been obtained near the fluid front. For each trial location of the fluid front ℓ_f, the algorithm determines the corresponding crack width w and fluid pressure p_f using Newton's iteration.

### 4.2. Hydraulic fracture without fluid lag, P&W scheme

The XFEM-ILSA algorithm with the *P&W* scheme was used in Gordeliy and Peirce (2013b) to model planar plane strain fracture propagating in viscosity-, toughness-, and transition- propagation regimes. The modifications developed in this paper to model non-planar fractures are described below.

4.2.1. The XFEM solution

In the *P&W* scheme, the XFEM solution is represented as a superposition of solutions that approximate the asymptotic width boundary condition in Σ_t (Eq. (11)) and the pressure boundary condition in Σ_c (Eq. (12)).

The crack discretization is similar to that in the $P \to W$ scheme. The crack, cutting N finite elements, is discretized into N straight-line crack elements $[s_i, s_{i+1}]$, $i = 1, \ldots, N$. The nodes s_i for $i = 1, \ldots, N$ are located at the finite element edges. For the XFEM-t scheme, the node $s_{N+1} = \ell$ is located at the crack tip. For the XFEM-s scheme, the crack is virtually extended beyond the crack tip to the farthest edge of the encompassing finite element, and the node s_{N+1} is located at the virtual crack tip (see Fig. 4).

The crack tip region Σ_t comprises one or more crack elements counting from the crack tip; the rest of the crack elements comprise the channel Σ_c. By analogy with the fluid lag problem, we denote by m the number of elements in the channel region for the *P&W* scheme, i.e., $\Sigma_c = \{s_1 \leq s \leq s_{m+1}\}$ and $\Sigma_t = \{s_{m+1} < s < \ell\}$. If there is one element in the crack tip region Σ_t, then $m = N - 1$.
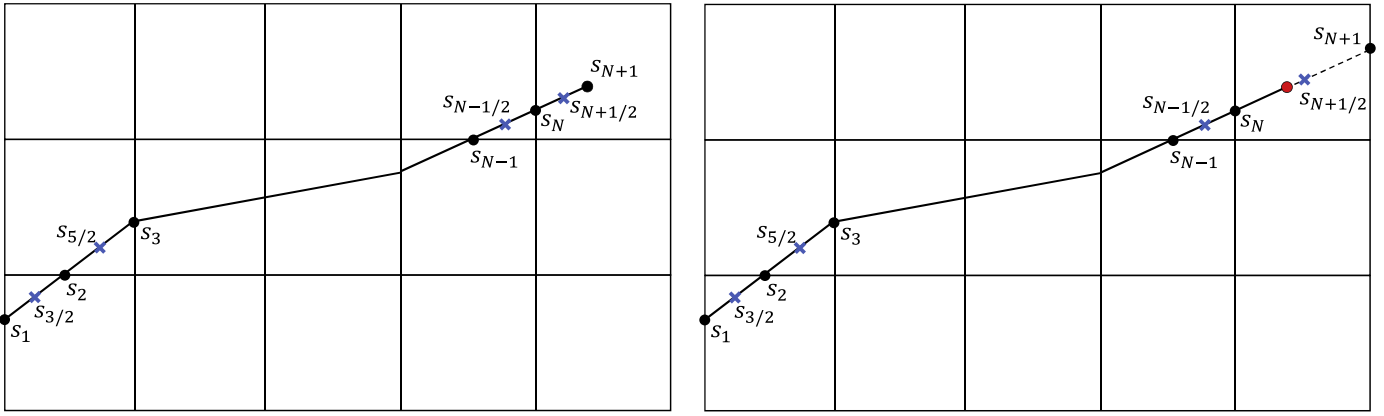
Fig. 4. Discretization of a crack within a finite element mesh, for the *P&W* XFEM-t (left) and *P&W* XFEM-s (right) schemes. Blue crosses denote the pressure nodes $s_{i+1/2}$ for $i = 1, \ldots, N$. For the XFEM-s scheme, the red circle denotes the location of the actual crack front. In the configuration shown, only one element belongs to the crack tip region Σ_t, which corresponds to the number of elements in the channel region $m = N - 1$. (For interpretation of the references to color in this figure legend, the reader is referred to the web version of this article.)

The pressure nodes $s_{i+1/2}$, for $i = 1, \ldots, m + 1$ (see Fig. 4), are defined for $i = 1, \ldots, m$ by Eq. (28), and for $i = m + 1$ by

$$s_{m+3/2} = \frac{s_{m+1} + s_{N+1}}{2} \tag{43}$$

The fluid pressure p_f in the channel ($s \in \Sigma_c$) is expanded in terms of the piecewise linear basis functions $h_{i+1/2}(s)$ associated with the nodal values $p_{i+1/2} = p_f(s_{i+1/2})$ using Eq. (30), which provides a C^0-continuous approximation of p_f within the channel Σ_c.

The XFEM approximation for the nodal widths in the channel is then obtained in the form

$$w_i = w(s_i, t) = \sum_{j=1}^{m+1} D_{ij} p_{j+1/2} + \omega_{t,i} + \omega_{\sigma,i}, \quad i = 1, \ldots, m + 1 \tag{44}$$

where D_{ij} is the influence matrix that expresses the effects of the pressure basis functions $h_{j+1/2}(s)$; and $\omega_{t,i}$ and $\omega_{\sigma,i}$ express, correspondingly, the effects of the crack-tip width and of the far-field stress (Appendix B.2).

The crack width in the tip region is given by the tip asymptote

$$w(s) = w_{\text{tip}}(s) \quad \text{for } s \in \Sigma_t \tag{45}$$

4.2.2. Discretization and solution of the fluid flow equations

The finite-volume discretization of the fluid-flow equations in the *P&W* scheme is similar to that used in the $P \to W$ scheme in Section 4.1.2. This discretization was given in Gordeliy and Peirce (2013b) for a plane strain fracture. The channel elements are treated similarly to the fluid-filled elements in the $P \to W$ scheme. The main difference in the discretization for the *P&W* scheme, is the use of the crack-tip asymptote in the crack-tip region Σ_t.

The volume of fluid in the tip region Σ_t is computed using the crack tip asymptote:

$$\text{Vol}_{m+1} = 2\pi \int_{s_{m+1}}^{\ell} r w_{\text{tip}}(s) ds \tag{46}$$

Similarly, the volume of fluid, present at time t_0, is computed analytically using the crack tip asymptote for those elements that were in the tip region at time t_0. For the tip region $[s_{m+1}, \ell]$, by virtue of the boundary condition (18) at the fracture front, the finite volume approximation becomes

$$\left[\text{Vol}_{m+1} - \text{Vol}_{m+1}^o \right] = 2\pi \Delta t \, r_{m+1} q_{m+1} \tag{47}$$

The equations for the elements in the channel Σ_c are similar to Eqs. (34)–(36). The volume Vol_k for $k \leq m$ is defined by Eq. (33).

For a given trial crack front ℓ at time t, the *P&W* scheme determines the $(m + 1)$-vector of nodal crack widths $\mathbf{w} =$

$(w_1, \ldots, w_{m+1})$ and the $(m + 1)$-vector of nodal fluid pressures $\mathbf{p} = (p_{3/2}, \ldots, p_{m+3/2})$. The elasticity equations (44) are used to express the nodal crack widths in terms of the nodal pressures, and the system of $(m + 1)$ nonlinear equations, resulting from the finite-volume discretization of the Reynolds equation, is solved for the nodal pressures $\mathbf{p} = (p_{3/2}, \ldots, p_{m+3/2})$ using Newton iteration.

4.3. Fracture propagation

4.3.1. Fracture propagation direction

When the solutions for the fracture front, fluid pressure, crack width, and fluid front have been obtained at time t_0, the direction of fracture propagation for the next time step, $t = t_0 + \Delta t$, is determined using the propagation criterion of Erdogan and Sih (1963). We recall the polar coordinates (ρ, θ) introduced at the fracture tip, in which $\theta = 0$ corresponds to the existing crack-tip orientation. For a homogeneous intact elastic material around the crack tip, the criterion in Erdogan and Sih (1963) states that the crack grows at an angle θ for which the hoop stress $\sigma_{\theta\theta}$ is maximized or equivalently when the shear stress is zero, $\sigma_{\rho\theta} = 0$. Such an angle θ can be found from the mode I and II stress intensity factors using Eq. (22). To find the stress intensity factors, one can use the interaction energy integral (e.g. Gosz and Moran, 2002) which is related to a decomposition of the *J*-integral (Rice, 1968b) for a mixed-mode fracture.

However, in this work we investigate an alternative approach in which the stresses are computed numerically at a number of benchmark points ahead of the crack tip and the angle θ, for which $\sigma_{\theta\theta}$ is maximized or $\sigma_{\rho\theta}$ is zero, is determined. In Fries and Baydoun (2012) and Baydoun and Fries (2012), this approach was successfully used to predict the direction of fracture growth in an XFEM model and was found to be simple to implement and to provide a straightforward extension to 3D.

The new crack direction is found by computing the shear stress $\sigma_{\rho\theta}(\hat{\rho}, \theta)$ at a number of points distributed on a circle of a small radius $\hat{\rho}$ from the crack tip, and finding the angle $\theta = \hat{\theta}$ for which the shear stress is zero:

$$\sigma_{\rho\theta}(\hat{\rho}, \hat{\theta}) = 0 \tag{48}$$

For a fracture propagating in a homogeneous intact elastic material and dominated by mode I (opening), the points are distributed in the interval $\theta \in (-72°, 72°)$. These margins for θ agree with the observation that for a mixed-mode crack, the direction of crack deflection is expected to be within about 70.5° (Erdogan and Sih, 1963). (The range of values of the angle (22) falls within the
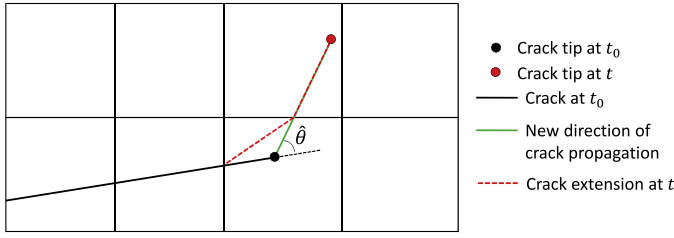
Fig. 5. Extension of the crack within a finite element mesh from its configuration at t_0 to the new configuration at t.

margins $\theta \in (-70.5°, 70.5°)$ for varying K_{II}/K_I. See also Fig. 5 in Erdogan and Sih (1963).) If multiple values of θ are found that satisfy Eq. (48), the value $\hat{\theta}$ is chosen for which the hoop stress $\sigma_{\theta\theta}$ is the largest.

If the radius $\hat{\rho}$ is sufficiently small, such that the stress field ahead of the crack tip within a distance $\hat{\rho}$ can be assumed to be dominated by the square-root singularity $\rho^{-1/2}$, the propagation direction found from Eq. (48) should be relatively independent of $\hat{\rho}$. A numerical example, investigating the dependence of the propagation direction on the distance $\hat{\rho}$, is considered in Section 5.2.5.

The crack is extended from its configuration at t_0 to the new configuration at t as shown in Fig. 5. The new crack trajectory is modified in the element containing the previous location of the crack tip so that the crack kinks are located at the edges of the finite element mesh.

Note that the XFEM-s scheme (the scheme with the sign enrichment only) does not capture the singular stress near the fracture tip, due to the lack of the crack-tip enrichment in this scheme. Although it is an efficient alternative to the fully crack-tip enriched model, the XFEM-s scheme may or may not provide an accurate prediction for the fracture propagation direction if this direction is determined from the stress ahead of the crack tip for a brittle fracture. Therefore, to ensure the accuracy of the fracture path obtained in the XFEM-s simulation, after the solution for a particular time step has been obtained using the XFEM-s scheme, the stress ahead of the fracture tip can be computed using the full crack-tip enrichment.

4.3.2. Implicit level-set algorithm

Once the direction of crack propagation for the time step t has been found, the extension of the fracture front along that direction is determined using the ILSA scheme (Peirce and Detournay, 2008). The ILSA scheme determines the fracture front location ℓ such that the fracture width near the crack tip, obtained from the coupled elasto-hydrodynamic equations, is compatible with the crack-tip asymptote. The application of the ILSA to model mode-I fracture propagation in the *P&W* scheme was described in the XFEM model in Gordeliy and Peirce (2013b) and is used here without modification. Below we present the use of the ILSA for the mixed-mode fracture propagation in modes I and II, for the $P \rightarrow W$ scheme.

At time t, the ILSA scheme iterates on the location of the fracture front ℓ. Consider a trial value $\ell^{(i)}$ at front iteration i. Let us consider a node s_K near the crack tip, e.g. with $K = N - 1$. It is assumed that the crack tip asymptote is valid at the node s_K.

For the current trial value of the fracture length $\ell^{(i)}$, the solution of the elasto-hydrodynamic equations determines the nodal crack widths in the channel, including the nodal crack width w_K and the ride v_k at the node s_K. We denote by $\mathcal{T}_K = -(\ell - s_K)$ the signed distance from the point s_K to the true fracture front location ℓ. The mixed-mode asymptote (21), applied at the node s_K, yields the following condition:

$$F(w_K, v_K) = \frac{K'}{E'}(-\mathcal{T}_K)^{1/2} \tag{49}$$

where $F(w_K, v_K) = \cos \frac{\hat{\theta}_K}{2} \left(w_K \cos^2 \frac{\hat{\theta}_K}{2} - \frac{3}{2} v_K \sin \hat{\theta}_K \right)$, v_K is the tangential displacement jump at node s_K, and the angle $\hat{\theta}_K$ is found from

$$\hat{\theta}_K = 2 \arctan \left(\frac{1 \pm \sqrt{1 + 8\eta^2}}{4\eta} \right), \quad \eta = \frac{v_K}{w_K} \tag{50}$$

(Note that the angle $\hat{\theta}_K$ in Eq. (50) is an estimate of the angle $\hat{\theta}$ for the fracture propagation direction at the next time step.)

Eq. (49) is inverted to compute the signed distance $\mathcal{T}_K$:

$$\mathcal{T}_K = -\left(\frac{E'}{K'} F(w_K, v_K) \right)^2 \tag{51}$$

Then the fracture front is updated for the next ILSA iteration as follows:

$$\ell^{(i+1)} = s_K - \mathcal{T}_K \tag{52}$$

This process is repeated until convergence in ℓ is achieved, at which stage the crack width w_K and the location of the fracture front ℓ are compatible with the tip asymptote.

4.4. Summary of the algorithm

The summary of the algorithm for one time step, $t = t_0 + \Delta t$, is shown below. For numerical computations, all the equations are scaled in order to improve the accuracy of numerical solutions, see Appendix C.

Given the solutions for the fracture front ℓ^o, the fluid pressure p_f^o, the crack width w^o, and the fluid front ℓ_f^o (for the problem with fluid lag) at time step t_0, and the new direction of fracture propagation $\hat{\theta}$:

- Find the crack length $\ell(t)$ using ILSA iterations, assuming the crack growth is in the propagation direction $\hat{\theta}$. For each value of the trial fracture length $\ell^{(i)}$:
  1. For the problem with fluid lag, locate the fluid front ℓ_f by solving Eq. (42). For each location of the trial fluid front ℓ_f, solve the coupled elasto-hydrodynamic equations to determine the crack width w and the fluid pressure p_f using Newton iteration.
  2. For the problem without fluid lag, solve the coupled elasto-hydrodynamic equations to determine the crack width w and the fluid pressure p_f using Newton iteration.
  3. Update the crack length $\ell^{(i+1)}$ for the next ILSA iteration. If $|\ell^{(i+1)} - \ell^{(i)}|$ is within a specified tolerance, break.
- For the new crack length $\ell(t)$, compute the shear stress $\sigma_{\rho\theta}(\hat{\rho}, \theta)$ on a circle of radius $\hat{\rho}$ around the crack tip. Find the angle $\theta = \hat{\theta}$ for which the shear stress is zero, Eq. (48). The angle $\hat{\theta}$ provides the direction of fracture propagation for the next time step.

5. Numerical results

5.1. Fracture propagation in the viscosity-dominated regime

In this section we verify the results of the XFEM model against the analytical solution for the propagation of a radial (penny-shaped) fracture in the viscosity-dominated regime (Savitski and Detournay, 2002). This analytical solution corresponds to the so-called "M-vertex" solution. The far-field stresses are assumed to have an axisymmetric distribution with $\sigma_{rr}^\infty = 70$ MPa and $\sigma_{zz}^\infty = 60$ MPa. The rock is characterized by $E = 35$ GPa and $\nu = 0.2$. The fluid, having a viscosity of $\mu = 0.1$ Pa.s, is assumed to be injected at a constant rate $Q = 0.026$ m^3/s. The initial fracture is taken as a penny-shaped crack of radius approximately $R = 1$ m, with the
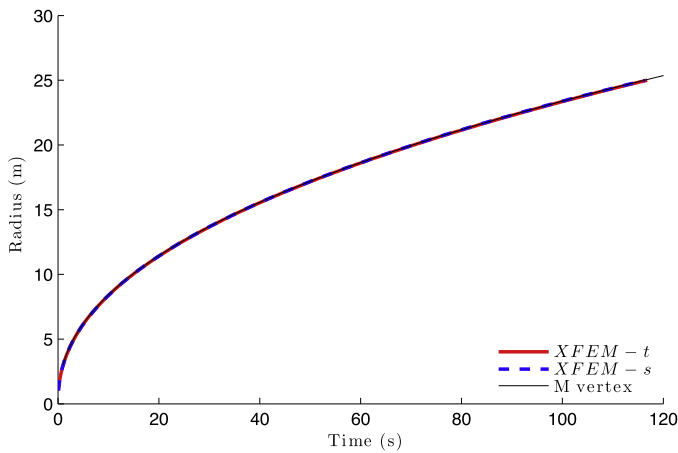
Fig. 6. Evolution of fracture radius, for a radial fracture propagating in the viscosity-dominated regime.

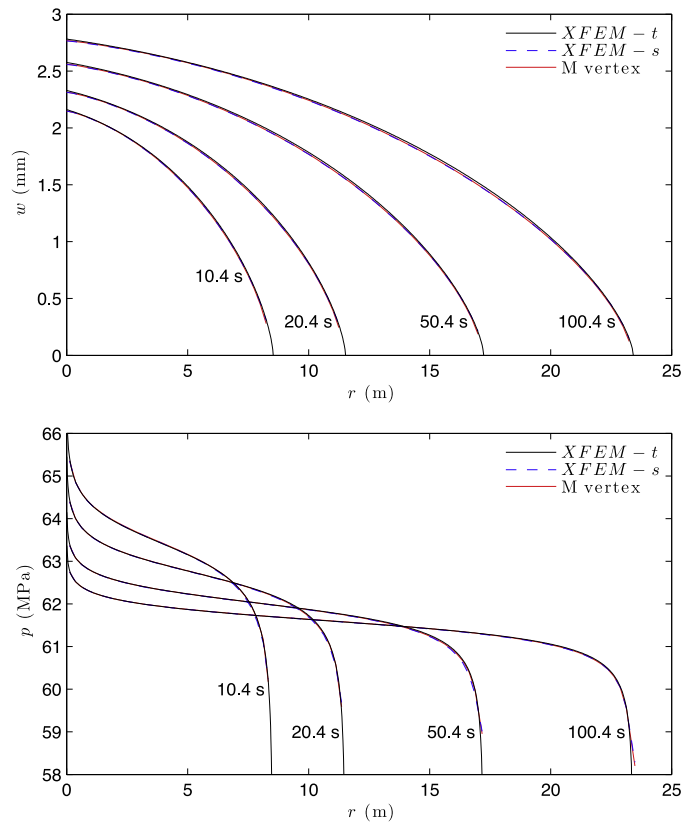**Fig. 7.** Crack width and fluid pressure at times $t = 10.4$ s, 20.4 s, 50.4 s, and 100.4 s, for a radial fracture propagating in the viscosity-dominated regime.

initial solution set to the M-vertex analytical solution (Savitski and Detournay, 2002). The wellbore is approximated as a point-source. The planar radial fracture is assumed to propagate in an infinite domain.

The XFEM results for this example were obtained using the *P&W* XFEM-t scheme (the scheme with the full crack-tip enrichment, with the tip asymptote used in the XFEM weak form) and the *P&W* XFEM-s scheme (the scheme with the sign enrichment only, with the tip asymptote imposed in the XFEM in a weak sense). The computational domain in cylindrical coordinates was defined by $0 \le r \le 25$ m, -6.38 m $\le z \le 6.62$ m. The domain was discretized into a structured mesh of 5200 quadrilateral finite elements of dimensions 0.25 m $\times$ 0.25 m. Along the boundary $\{r = 0\}$, the conditions of axisymmetry were enforced; along the rest of the domain boundary, infinite elements were employed (Section 3.3). The initial fracture geometry was defined by $0 \le r \le 1.0001$ m, and $z = 0$. Figs. 6 and 7 show a comparison of the XFEM results with the M-vertex analytical solution (Savitski and Detournay, 2002) for the fracture radius, crack width and the fluid pressure in the fracture. The XFEM results show an excellent agreement with the analytical solution. The XFEM-s scheme, with only sign enrichment representing the crack, provides an efficient and sufficiently accurate alternative to a crack-tip enriched XFEM model, due to the use of the crack tip asymptote in the weak formulation of the XFEM. By virtue of the infinite elements, the XFEM results match the infinite-space solution even for times at which the fracture tip approaches the interface between the finite and infinite elements (at $r = 25$ m).

5.2. Near-surface fracture propagation with fluid lag

In this section, we compare the XFEM results with the results of laboratory experiments for bowl-shaped hydraulic fractures (Bunger et al., 2013). The results of the displacement discontinuity model OribiC, compared to the laboratory data in Bunger et al. (2013), are included as well. We summarize below the details of the experiments required for setting up the XFEM model and interpreting its results. For complete details of the experiments, the reader is referred to the work of Bunger et al. (Bunger, 2005; Bunger et al., 2004; 2013).

5.2.1. Summary of experiments and DDM simulations from Bunger et al. (2013)

We consider five of the six experiments presented in Bunger et al. (2013) (*ab5, c6m1, pg1, pg4, pg2*). The details of the experiments, considered in this paper, are summarized in

Table 1. In each experiment, a specimen, made of either polymethyl methacrylate (PMMA) or glass, was subject to axisymmetric lateral (confining) stress σ_{rr} and hydraulically fractured, as shown in Fig. 3 in Bunger et al. (2013). The fractures initiated at manufactured notches at the end of the wellbore and propagated towards the free surface of the specimens. The fractures developed bowl-shaped trajectories. It was confirmed that the trajectories correspond to the ratio $\chi = \frac{|\sigma_{rr}|\sqrt{H}}{K_{Ic}}$, in accordance with the hypothesis earlier suggested by Zhang et al. (2002), where H is the distance from the initial crack to the free surface.

In tests *c6m1, pg1, pg4*, and *pg2*, the specimens were cylindrical, with diameter 145 mm and thickness 60 mm. Each specimen was put in a Hoek-type pressure cell, which was used to apply the lateral stress σ_{rr} to the specimen. In test *ab5*, the specimen was a rectangular block of dimensions 360 mm x 400 mm x 120 mm thick. In tests *pg1* and *ab5*, no lateral load was applied to the specimens. (The effect of the atmospheric pressure was neglected in the DDM model, and the lateral load for tests *pg1* and *ab5* was set to $\sigma_{rr} = 0$.) Table 1 lists the stress value which is representative of the stress σ_{rr} applied in each experiment and which was used in the DDM model in Bunger et al. (2013).

Each specimen contained a borehole (7.4-mm diameter in PMMA, 8.0-mm diameter in glass) with a steel injection tube (6.4 mm outer diameter) cemented in the borehole using epoxy. The fracture initiated at a circular notch, of approximately 12 mm diameter, manufactured at the end of the wellbore. In tests *pg1, pg4*, and *pg2* (in glass), significant fluid lag was observed between the fracture and fluid fronts. In tests *ab5* and *c6m1* (in PMMA), no fluid lag was observed, due to a relatively larger dimensionless toughness associated with these tests.

The experiments were modeled in Bunger et al. (2013) by using a hydraulic fracture model OribiC, based on the axisymmetric dis-

Table 1
Parameters of the laboratory experiments of Bunger et al. (2013) considered in this paper.

Test	Material	χ	$\|\sigma_{rr}\|$ (MPa)	E (GPa)	ν	K_{Ic} (MPa m$^{1/2}$)	μ (Pa s)	Q_0 (ml/s)	H (mm)
ab5	PMMA	0	0	3.3	0.4	1.37	2.5	0.1	15
c6m1	PMMA	0.5	6.3	3.3	0.4	1.37	1.63	0.12	12
pg1	Glass	0	0	62.8	0.2	0.64	0.16	0.0002	12
pg4	Glass	0.5	2.9	62.8	0.2	0.64	0.14	0.08	12
pg2	Glass	1	5.8	62.8	0.2	0.64	0.12	0.08	12

placement discontinuity method (Gordeliy and Detournay, 2011). The specimens were modeled as an elastic half-space without a wellbore. The fractures were modeled as axisymmetric (bowl-shaped), with the fluid injected from a point source at the center of the fracture. While a nominally constant injection rate Q_0 was supplied to the wellbore in the experiments (given in Table 1), the rate of fluid entering the fracture was time-dependent due to the compressibility of the injection system. To account for the time-dependent fluid rate entering the fractures, the OribiC model used piecewise-linear time-dependent injection rates chosen such that the injected volume would correspond to the recorded injected volume from the experiments.
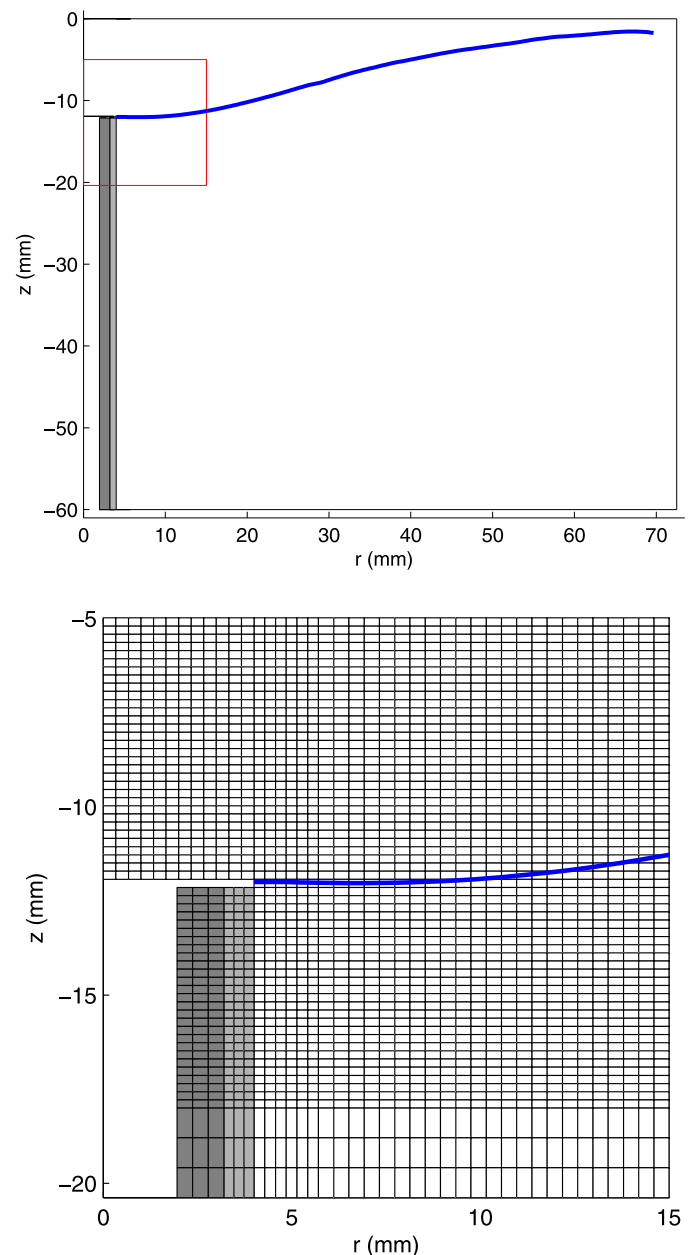
5.2.2. XFEM model

The XFEM results have been obtained using the $P \rightarrow W$ XFEM-t scheme. The mixed-mode tip asymptote (21) was used in the ILSA algorithm outside of the XFEM solver, to track the fracture front with time.

For the XFEM simulations for tests *c6m1*, *pg1*, *pg4*, and *pg2*, the computational domain represents the cylindrical specimen having a radius of 72.5 mm and thickness of 60 mm, consistent with the specimen dimensions used in the experiments. For the XFEM simulation for test *ab5*, the computational domain represents an equivalent cylindrical specimen with a radius of 180 mm and thickness of 120 mm. As an example, the computational domain for test *pg4*, with the background finite element mesh, is shown in Fig. 8.

The domain is discretized using a structured rectangular mesh in cylindrical coordinates. The wellbore includes the steel tube (with Young's modulus 200 GPa, Poisson's ratio 0.3) and the epoxy adhesive layer (with Young's modulus 2 GPa, Poisson's ratio 0.4), modeled as elastic materials. The effects of any inelastic behavior of the wellbore system are assumed to be negligible. The initial radial notch is represented by an initial crack having dimensions corresponding to the initial notch size in the experiments.

The outer cylindrical surface of the specimen (the cylindrical surface on the right, in Fig. 8 (top)) is subject to the normal confining stress $\sigma_{rr} = -\frac{\chi K_{Ic}}{\sqrt{H}}$ and zero shear stress, $\sigma_{rz} = 0$. (The tension-positive convention for stresses is employed.) The surfaces parallel to the initial notch (top and bottom surfaces of the specimen, in Fig. 8 (top)) are traction-free. (This assumption is discussed in the next section.) The surface of the wellbore is subject to a uniform wellbore pressure, equal to the fluid pressure $p_f(0, t)$ at the fracture inlet, and zero shear stress. Along the boundary at $r = 0$, axial symmetry requires that $u_r = 0$. To remove rigid body motion, a zero displacement component u_z, $u_z = 0$, is enforced at the corner node of the outer cylindrical surface, corresponding to $r = 72.5$ mm and $z = 0$.

The initial cracks were subject to a uniform pressure. The problem parameters were taken according to the values in Table 1 (except for the injection rates). The same time-dependent injection rates $Q(t)$ were used in the XFEM simulations as the ones used in the corresponding OribiC simulations, given in Fig. A3 in Bunger et al. (2013).

Fig. 8. XFEM model of the cylindrical specimen with computed fracture path for test *pg4*: computational domain with a square inset area marked by a red line (top) and mesh detail around the initial notch in the square inset area (bottom). The fracture path is shown by the blue line; the steel injection tube and the epoxy liner along the wellbore are shaded in dark grey and light grey color, respectively. (For interpretation of the references to color in this figure legend, the reader is referred to the web version of this article.)
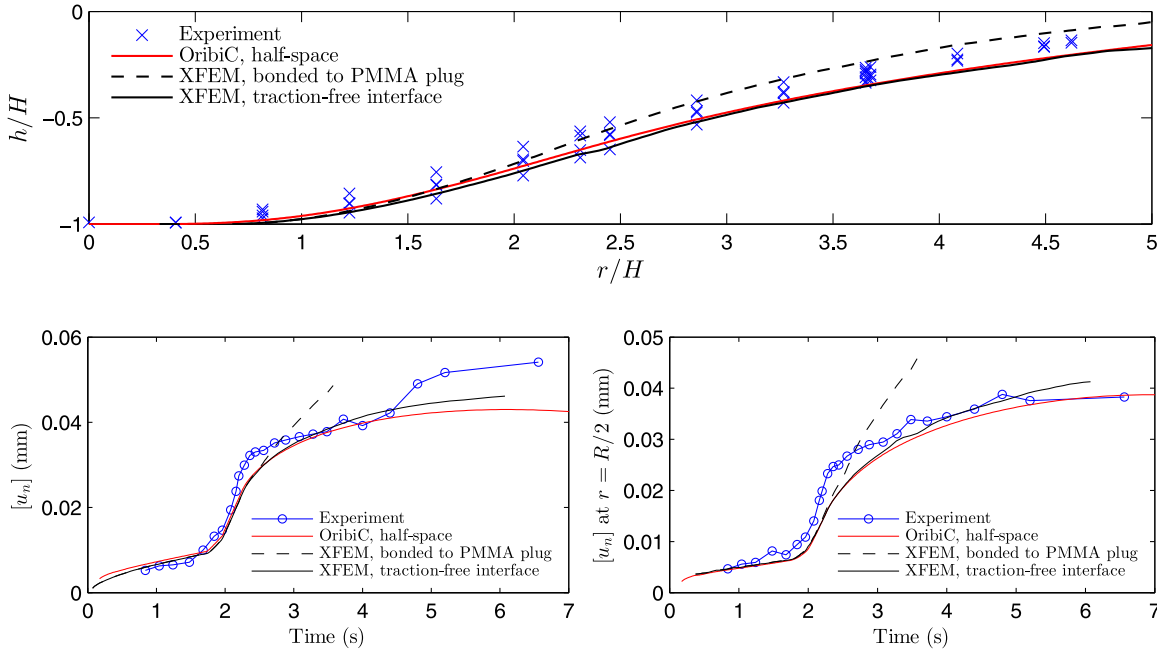
Fig. 9. Results for test *pg4*, obtained in the experiment and computed with the DDM model OribiC (Bunger et al., 2013), and computed with the XFEM using different boundary conditions along the interface between the glass specimen and the plug filling the Hoek cell: fracture path (top), and crack opening at fracture inlet (bottom, left) and half-way into the fracture (at $r = R/2$) (bottom, right).

5.2.3. Boundary conditions along the interface between two materials

In tests *c6m1*, *pg1*, *pg4*, and *pg2*, the specimen was put in a Hoek cell. To fill the back of the Hoek cell, a PMMA plug was inserted into the cell behind the specimen, as shown in Fig. 3 in Bunger et al. (2013). The specimen and the plug were not bonded, i.e., a gap could have existed between the specimen and the plug, while on the other hand, the specimen and the plug could have come into contact during the experiment.

For test *pg4,* we studied the effect of the boundary conditions along the interface between the glass specimen and the PMMA plug on the fracture shape and the fracture opening. The fracture width was compared at the fracture inlet and at half of the fracture radius, at $r = R/2$. Fig. 9 shows a comparison of the XFEM results obtained using two types of the boundary conditions: the PMMA plug bonded to the glass to form a bi-material specimen, and a traction-free surface along the interface between the glass specimen and the PMMA plug. (In the XFEM simulation with the PMMA plug bonded to the glass, the cylindrical PMMA plug had a 72.5 mm radius and 170 mm thickness. A zero displacement component u_z, $u_z = 0$, was enforced at the corner node of the mesh corresponding to $r = 72.5$ mm and $z = 0$, to remove rigid body motion. A normal confining stress $\sigma_{rr} = -\frac{\chi K_{Ic}}{\sqrt{H}}$ and zero shear stress, $\sigma_{rz} = 0$, were applied to the lateral cylindrical surface of the plug and of the specimen.) For comparison, Fig. 9 includes the OribiC results from Bunger et al. (2013), which were based on a half-space approximation of the specimen.

The interface boundary conditions have a significant effect on the fracture trajectory and the fracture opening. The XFEM result with the traction-free specimen boundary along the interface and the DDM results are in good agreement with the experimental data for the fracture opening. The fracture paths from all three simulations slightly deviate from the experimental result. We note that the XFEM result, assuming that the glass specimen and the PMMA plug are bonded, results in a deflection of the fracture path toward the free surface compared to the traction-free XFEM simulation and the DDM result. This is due to the significant contrast in the elastic properties of the PMMA plug and the glass specimen,
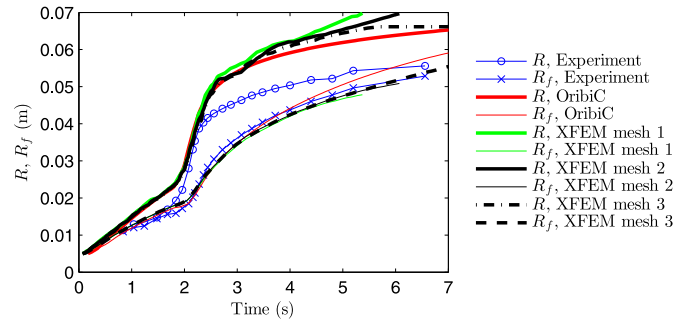

Fig. 10. Fracture and fluid fronts for test *pg4*, computed with the XFEM using three mesh levels.

which affects the orientation of principal stresses in the specimen bonded to the plug and causes the fracture path to deflect toward the free surface. As the result, the fracture opening is larger for the XFEM simulation with the PMMA plug bonded to the glass, in comparison to the other two simulations, and does not follow the behavior of the fracture width in the experiment.

The capacity of the XFEM to model a bi-material specimen thus enables us to discount any significant contact between the glass and the PMMA plug in the experiment. Therefore a zero-traction interface boundary condition is used in the following for all XFEM simulations for the tests *c6m1*, *pg1*, *pg4*, and *pg2*.

5.2.4. Convergence with mesh refinement

A level of mesh refinement, sufficient to compute the results with reasonable accuracy and within a reasonable computational time, was chosen by comparing the results for three mesh levels for test *pg4*. Figs. 10 and 11 show a comparison of the results obtained using 10,760 finite elements (mesh level 1, with $h_x \in \{0.43$ mm, 0.61 mm$\}$ and $h_y = 0.33$ mm, where $h_x \times h_y$ are the dimensions of a rectangular element in the subdomain of fracture propagation), 24396 finite elements (mesh level 2, with $h_x \in \{0.29$ mm, 0.40 mm$\}$ and $h_y = 0.22$ mm), and 43,489 fi-
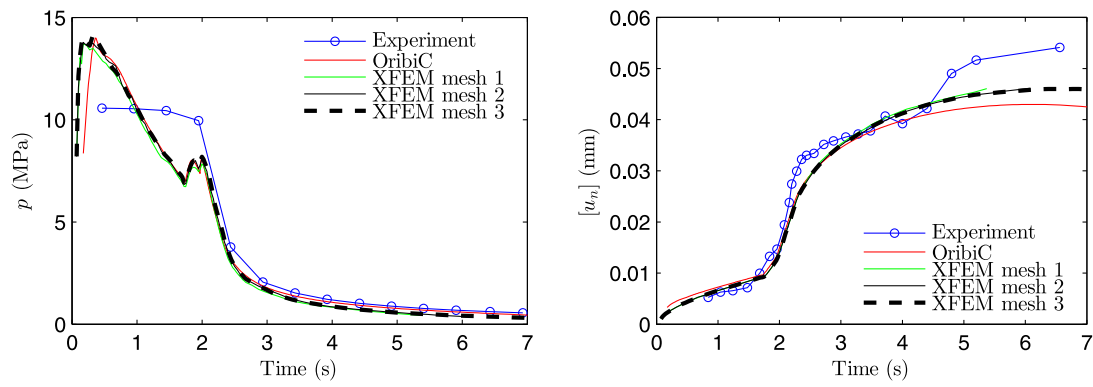
Fig. 11. Fluid pressure (left) and fracture width (right) at the fracture inlet for test *pg4*, computed with the XFEM using three mesh levels.
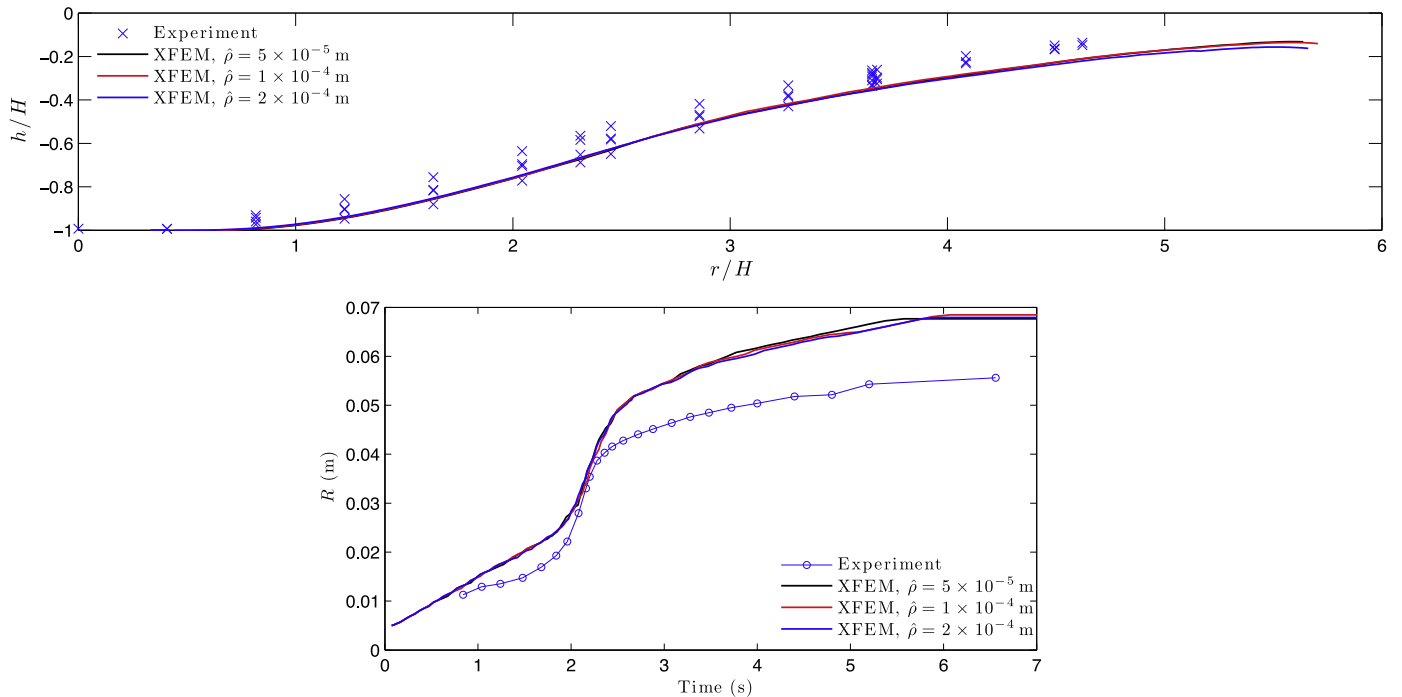

Fig. 12. Fracture path (top) and fracture radius (bottom) for test *pg4*, computed with the XFEM using three values of the distance $\hat{\rho}$ from the crack tip, at which the stress is computed.

nite elements (mesh level 3, with $h_x \in \{0.21\,\text{mm}, 0.30\,\text{mm}\}$ and $h_y = 0.16$ mm). The dimensions of all the finite elements were uniformly decreased from mesh level 1 to the mesh levels 2 and 3. A snapshot of the finite element mesh, corresponding to mesh level 2, is shown in Fig. 8 (bottom). Figs. 10 and 11 show that there is no significant difference between the results for the pressure, fracture width, and fluid front, for all three meshes. The largest difference between the solutions for the three meshes is observed in the fracture radius R in Fig. 10. With mesh refinement, the XFEM results for the fracture radius become closer to the OribiC result, which was obtained with constant-strength displacement discontinuity elements of length $\Delta s_{\text{OribiC}} = 0.12$ mm. (Both the XFEM and the DDM (OribiC) solutions overestimate the fracture front radius for this experiment.) Based on the comparison between the three XFEM solutions, the mesh level 2 is found to be sufficient and is used in the following simulations for tests *pg1*, *pg4*, and *pg2*. A similar mesh refinement level is used for the simulation for test *c6m1*. For test *ab5*, a coarser mesh is used due to the larger specimen size in this test.

The crack radius in the XFEM results in Fig. 10, for mesh levels 1 and 2, shows some ragged behavior. This can be attributed

to the mesh-dependence of the XFEM solution, since the crack radius for mesh level 3 shows a smoother growth. Another contributing aspect is the convergence of the solution for the crack-front. Note that the original ILSA algorithm of Peirce and Detournay (2008) employs the crack-width asymptote to explicitly define the boundary values of crack width near the fracture front within the discretization of the coupled equations for fluid flow and linearly-elastic solid deformation. This approach ties down the boundary values of the crack width near the crack tip and contributes to a fast convergence of the ILSA algorithm. However, since the mixed-mode tip asymptote does not provide an explicit asymptote for the crack width alone, it is not employed to set the boundary values of crack width near the fracture front within the discretization of the coupled fluid-solid equations. Therefore, for simulations of the mixed-mode propagation for laboratory tests, we have used the $P \to W$ scheme which is simple in implementation but does not enforce the crack-tip asymptote in the fluid flow and elasticity equations. Such a reduced ILSA algorithm has a slower convergence rate than the original ILSA approach.
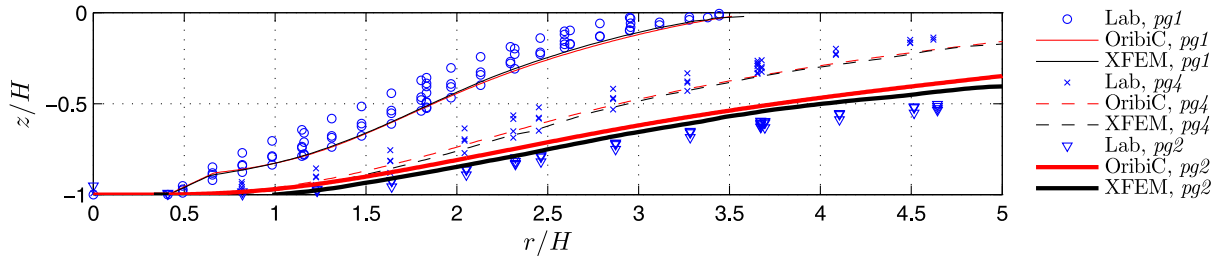
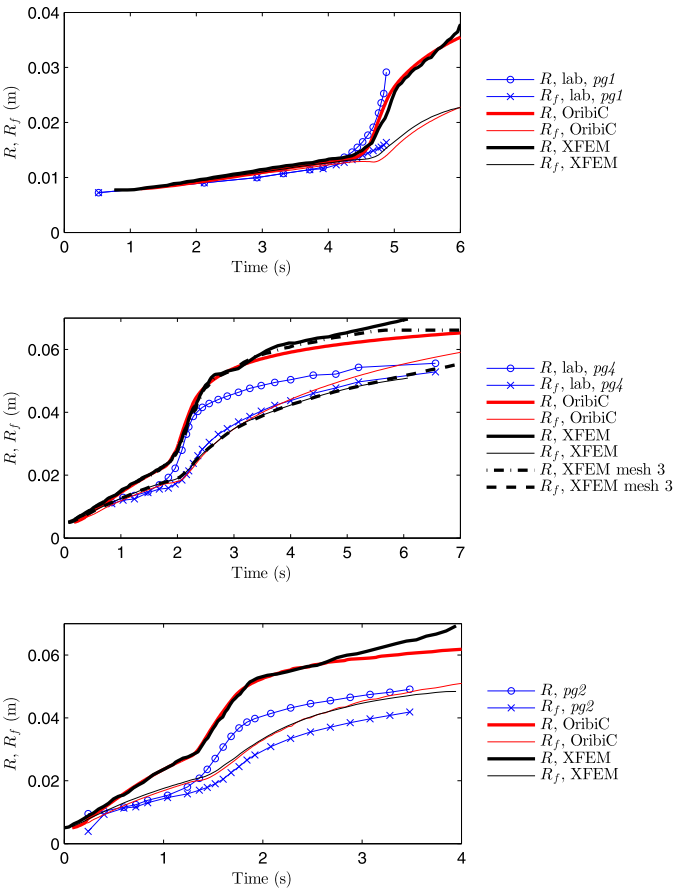**Fig. 13.** Fracture paths for glass specimens.

Fig. 14. Fracture and fluid fronts for glass specimens.

5.2.5. Dependence of crack propagation angle on the distance $\hat{\rho}$

To test the dependence of the crack propagation direction on the distance $\hat{\rho}$ from the crack tip, at which the stress is computed (Eq. (48)), we performed the XFEM simulations for test *pg4* with $\hat{\rho} = 0.2$ mm, 0.1 mm and 0.05 mm. The comparison of the results for the crack path and the fracture radius is shown in Fig. 12. There are no significant differences in the results for the three values of $\hat{\rho}$, except for the time when the fracture tip approaches the free surface. Near the surface, the smallest value of $\hat{\rho}$ results in a more accurate crack path. In the following XFEM simulations, $\hat{\rho} = 0.05$ mm is used.

5.2.6. Results for glass specimens

Figs. 13–15 show the XFEM results obtained for tests *pg1*, *pg4*, and *pg2* using mesh level 2.

Note that for test *pg1*, a small initial kink (shown by the change of the fracture curvature between $r/H = 0.4$ and $r/H = 0.64$ in Fig. 13) was introduced in both numerical models to be able to

match the crack path with the experiment. Similarly, an initial kink in the fracture path was introduced for test *ab5* in both numerical models, to be able to match the fracture path (Section 5.2.7). It was conjectured in Bunger et al. (2013) that the DDM model was not able to predict the initial sharp kinks in the crack paths for tests *pg1* and *ab5* (corresponding to $\sigma_{rr} = 0$) because it did not include the influence of the wellbore. However, we found that the XFEM model, which includes the wellbore configuration corresponding to the experiment, is also unable to match the crack path for tests *pg1* and *ab5* with the experiment, unless the initial kink was introduced.

The comparisons for the crack paths (Fig. 13), the fracture radius, and the fluid front location (Fig. 14), the fluid pressure, and the crack opening at the fracture inlet (Fig. 15) show that the XFEM results are in good agreement with both the experimental data and the DDM model. This comparison not only serves as a validation of the XFEM implementation presented in this paper, but also makes it possible to identify the effects of the differences between the XFEM and the DDM models in comparison to the experimental data. For test *pg2*, the XFEM predicts a fracture shape which is closer to the experimental results. This could be attributed to the effect of the finite domain and the pressurized wellbore in the XFEM model, in comparison to the half-space model with a point-source in the DDM model. In particular, in test *pg2* shown in Fig. 13, the fracture in the experiment daylighted at the outer cylindrical surface of the specimen (at $r = 72.5$ mm); therefore, the finite size of the specimen could be expected to have a significant impact on the fracture trajectory in this test. Naturally, the finite-domain model of the XFEM is more representative of this test than the half-space DDM model. As a result, the fracture shape from the XFEM simulation for test *pg2* is closer to the experimental result than that of the DDM model.

The fracture radius shown in Fig. 14 is captured by the XFEM model relatively well, and a better convergence to the results of the DDM model is expected upon mesh refinement (see Section 5.2.4). For test *pg4*, Fig. 14 includes the additional XFEM results obtained with the refined mesh (mesh level 3). Note that even though both numerical models overestimate the fracture radius, the fluid front radius R_f is captured well. For tests *pg1* and *pg4*, the XFEM prediction for the fluid front radius is in fact closer to the experimental data.

It should be noted that, for test *pg2* only, there is an error in the plot of the experimental data for the fracture and fluid fronts in Fig. 9 (bottom, left) in Bunger et al. (2013). The correct experimental data for R and R_f for test *pg2* correspond to those in Fig. 9 (bottom, left) in Bunger et al. (2013) multiplied by a factor 0.8. The correct experimental values for R/H for test *pg2* can also be obtained from the supplementary data in Appendix C of (Bunger et al., 2013).

Since the numerical models overestimate the fracture radius, the models overestimate the created fracture surface area. As a test, we have tried to increase the fracture toughness K_{Ic} in the XFEM model, in order to try to match the fracture radius R with
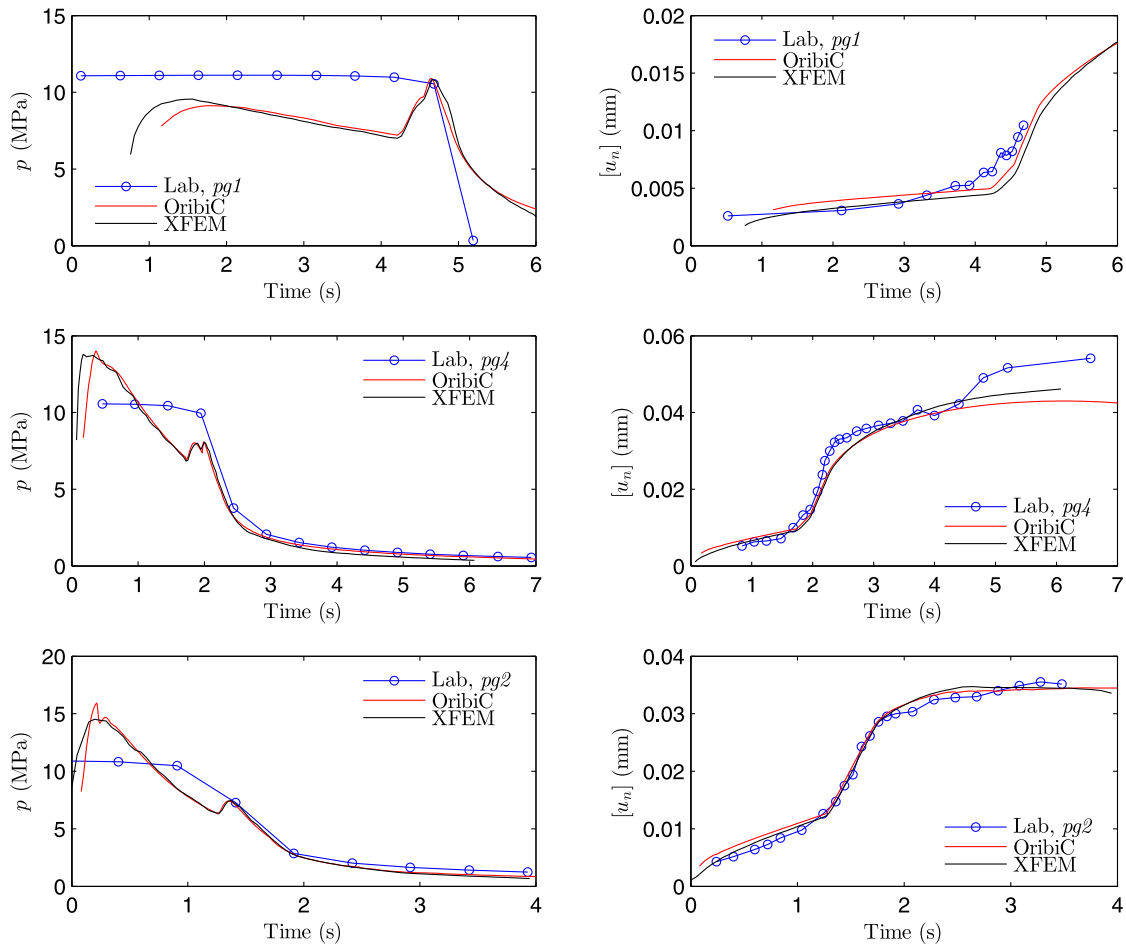
Fig. 15. Fluid pressure (right) and crack opening (left) at fracture inlet (at $r = 4$ mm), for glass specimens.
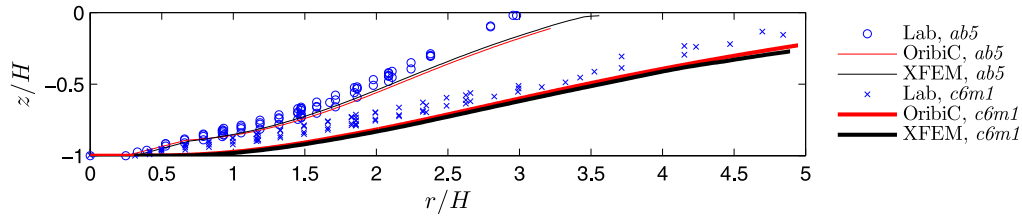

Fig. 16. Fracture paths for PMMA specimens.

the experimental data. Since the fracture trajectory depends on the ratio $\chi = \frac{|\sigma_{rr}|\sqrt{H}}{K_{Ic}}$, changing the fracture toughness K_{Ic} and/or the lateral stress σ_{rr} leads to a change in the crack path, unless these two quantities are changed proportionally. We were not able to find a unique pair of values (K_{Ic}, σ_{rr}), such that it would make it possible to consistently match the fracture radius and the fracture path for all three tests in glass (*pg1*, *pg4*, and *pg2*).

There is no significant difference between the results of the XFEM and DDM models for the fluid pressure and the crack opening at the fracture inlet (Fig. 15). The results of both models show excellent agreement with the experimental data.

5.2.7. Results for PMMA specimens

In this section we present the XFEM results for tests in the PMMA samples (tests *ab5* and *c6m1*). No fluid lag was observed in these tests in the laboratory. The fractures in the PMMA specimens lost their axial symmetry during the experiments and became significantly asymmetric ("egg-shaped") once the fracture ra-

dius was sufficiently large (Bunger et al., 2013). This symmetry-breaking is typical of toughness-dominated propagation (Bunger, 2005; Gao and Rice, 1985). The fracture radius R, reported from the experiment, was computed as the average radius over several radial directions from the injection point (Bunger et al., 2013).

We use the same XFEM model as the one used for the glass specimens, i.e., the fluid front is not forced to coincide with the fracture front. An initial kink in the fracture path was introduced for test *ab5* in the XFEM model as well as in the OribiC model, to be able to match the fracture path.

Figs. 16–18 show the results for the fracture path, the fracture radius and the fluid front radius, the wellbore pressure, and the fracture width at the fracture inlet and sampled at half of the fracture radius (at $r = R/2$). The XFEM results are again in good agreement with the experimental data and the OribiC results, except that the results of both numerical models overestimate the fracture opening. The fracture fronts and the fluid fronts coincide in both XFEM simulations, in agreement with the laboratory observa-
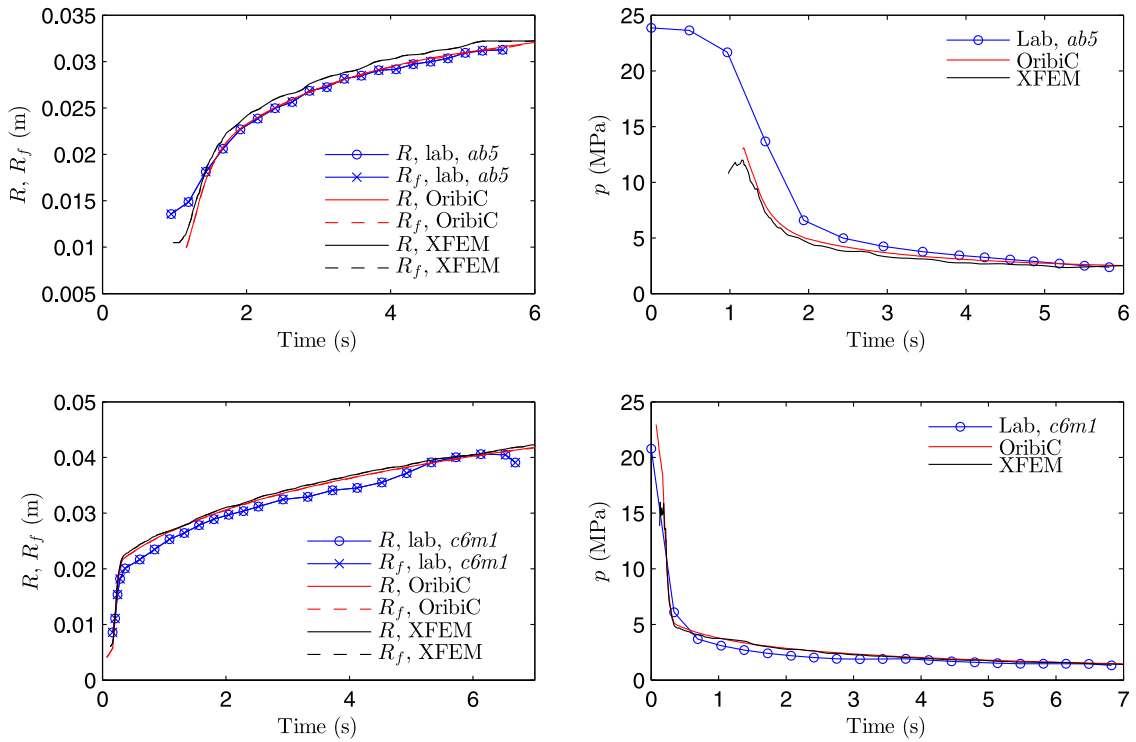
Fig. 17. Fracture and fluid fronts (right) and fluid pressure at fracture inlet (left), for PMMA specimens.
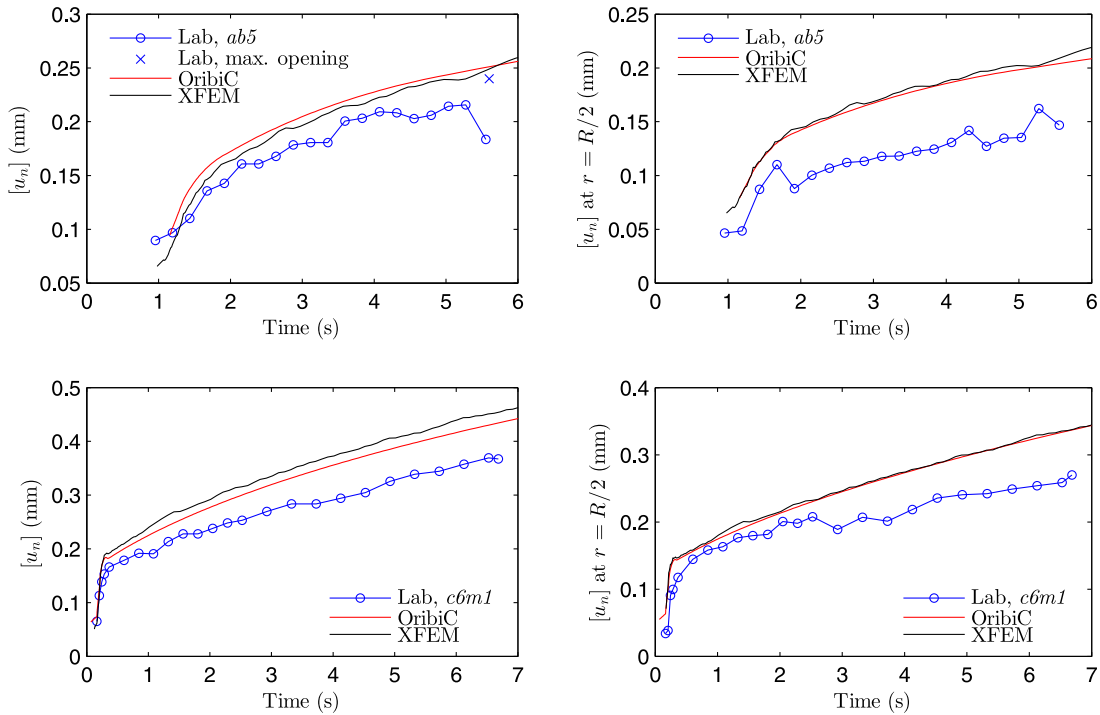

Fig. 18. Crack opening at fracture inlet (left) and half-way into the fracture (at $r = R/2$) (right), for PMMA specimens. For test *ab5* (top left), the cross mark depicts the maximum fracture opening observed in the experiment at time $t \approx 5.6$ s.

tions. Note that the results for test *ab5* are slightly ragged, which can be due to the coarser mesh used for this test. (The finite element size for test *ab5* was about twice that for the mesh used for the XFEM simulation for test *c6m1*.)

It was noted in Bunger et al. (2013) that the OribiC modeling results for the PMMA specimens overestimated the fracture opening by as much as 20%. This overestimation can be directly linked to

the fact that the fractures in the PMMA samples were loosing their symmetry during the experiments and were becoming egg-shaped once the fracture radius was sufficiently large, as shown in Fig. 6 in Bunger et al. (2013) and Fig. 6.11 in Bunger (2005). As the result of this shape change, the location of the maximum fracture opening was no longer at the inlet but shifted towards the largest radius, as can be seen from Fig. 6.11 in Bunger (2005). Therefore, for

the same injected volume and the same average fracture radius R, the fracture opening at the center of a radially symmetric fracture should be larger than the fracture opening at the injection point of an asymmetric fracture. In other words, it is to be expected that the inlet crack width obtained in the axisymmetric XFEM and DDM models should be larger than the inlet crack width observed in the laboratory experiments when the fractures became egg-shaped. In fact, at time $t \approx 5.6$ s for test *ab5*, the magnitude of the maximum fracture opening in the experiment in Fig. 6.11 in Bunger (2005) is roughly 0.24 mm (while the fracture opening at the injection point is roughly 0.18 mm). The modeling results for the inlet crack width at time $t \approx 5.6$ s (Fig. 18) are roughly 0.25 mm, i.e. very close to the maximum fracture opening observed in the experiment (shown in Fig. 18 by a cross). Thus, the XFEM and the DDM results for the fracture opening can be considered to be consistent with the laboratory experiments for tests *ab5* and *c6m1*.

6. Conclusions

In this paper we have further developed the 2D plane strain hydraulic fracture XFEM model (Gordeliy and Peirce, 2013b) to enable it to model nonplanar axisymmetric hydraulic fractures. Nonplanar fractures are represented by using the hybrid explicit-implicit crack description of Fries and Baydoun (2012). The fracture propagation in the mixed mode (I–II) is modeled within the framework of the implicit level-set algorithm (Peirce and Detournay, 2008). The direction of fracture propagation is found according to the propagation criterion of Erdogan and Sih (1963).

We verified the results of the axisymmetric XFEM formulation against the analytical solution for propagation of a radial fracture in the viscosity-dominated regime. The XFEM results show excellent agreement with the analytical solution (Savitski and Detournay, 2002).

We have validated the axisymmetric XFEM HF simulator against the results of laboratory experiments and the results of a DDM HF model. The comprehensive comparison of the results from the XFEM with the results from the DDM and with the laboratory data reveals which components of the present XFEM model (that are missing in the DDM model) affect the fracture characteristics. In particular, we found that for the conditions of these experiments, the wellbore and the finite lateral boundary of the specimen, explicitly represented by the XFEM, did not have a significant impact on the numerical results, since the two models predicted similar results. On the other hand, the ability of the XFEM to model a finite domain and inhomogeneous elastic materials made it possible to discount a bi-material contact between the specimen and a plug used in the experiments performed in the Hoek cell. The new algorithm to track the fluid front, implemented in the XFEM model, made it possible to obtain fluid front results that are closer to the experimental values than the results from the DDM model. Finally, with mesh refinement in the XFEM, the XFEM results for the fracture radius converge to the DDM results.

Appendix A. XFEM formulation for a nonplanar fracture

Below we present the XFEM solution for the elastic deformation of the medium. The formulation is based on the previous work (Gordeliy and Peirce, 2013b; 2015), with new components included to represent a non-planar fracture.

For all examples in this paper, at each point on the domain boundary, $\boldsymbol{x} \in \Gamma$, either a zero displacement $u_i(\boldsymbol{x}) = 0$ or a given boundary traction $t_i(\boldsymbol{x}) = t_i^*(\boldsymbol{x})$ is prescribed, in each coordinate direction ($i = r, z$). We denote those parts of Γ with prescribed displacement components, $u_i(\boldsymbol{x}) = 0$, as $\Gamma_{u, i}$, and those parts of Γ with prescribed traction components, $t_i(\boldsymbol{x}) = t_i^*(\boldsymbol{x})$, as $\Gamma_{t, i}$.

The computational domain V is discretized into a finite element mesh comprising a set of nonoverlapping quadrilateral elements. The displacement in V is approximated by functions in the trial space $\mathscr{U}_{\mathbf{u}}^h = \left\{ \mathbf{u}^h \mid \mathbf{u}^h \in U, u_i^h = 0 \text{ on } \Gamma_{u,i}, i = 1, 2 \right\}$, and variations $\mathbf{v}^h$ are taken from the test space (which is the same as the trial space, consistent with a Galerkin formulation), $\mathbf{v}^h \in \mathscr{U}_{\mathbf{u}}^h$. In the description that follows, $U = H^{1h} \times H^{1h}$ is a finite-dimensional subspace of the Sobolev space $H^1(V \backslash \Sigma) \times H^1(V \backslash \Sigma)$ that consists of the shape functions representing the discretization $\mathbf{u}^h$. The shape functions for the XFEM-t scheme and the XFEM-s scheme are discussed in Section 3.1. The domain V includes the crack Σ. The domain $V \backslash \Sigma$ that does not contain the crack is assumed to be piecewise Lipshitz. The test and trial functions are chosen so that they are discontinuous at the crack Σ in a direction normal to the crack.

A.1. Weak formulation for the P → W scheme

For a test function $\mathbf{u}^h$, the corresponding strain $\boldsymbol{\varepsilon}(\mathbf{u}^h)$ can be computed from (4), and the corresponding stress can be obtained from Hooke's law (3) to yield $\boldsymbol{\sigma}(\mathbf{u}^h) = \mathcal{C} : \boldsymbol{\varepsilon}(\mathbf{u}^h)$. The discretized weak formulation of the elasticity problem corresponding to the $P \to W$ scheme follows (Fries, 2008) and seeks to find $\mathbf{u}^h \in \mathscr{U}_{\mathbf{u}}^h$ such that for all $\mathbf{v}^h \in \mathscr{U}_{\mathbf{u}}^h$

$$0 = \int_{V \backslash \Sigma} \boldsymbol{\varepsilon}(\mathbf{v}^h) : \boldsymbol{\sigma}(\mathbf{u}^h) \, dV - \sum_{i=1,2} \int_{\Gamma_{t,i}} v_i^h t_i^* dA$$

$$+ \int_{\Sigma} [[\mathbf{v}^h]] \cdot \left((\sigma_n^\infty - p_f) \mathbf{n} + \sigma_s^\infty \mathbf{s} \right) dA \tag{A.1}$$

In the above, $[[\mathbf{v}]] = (\mathbf{v}^+ - \mathbf{v}^-)$ denotes the jump of $\mathbf{v}$ across the crack. Note that the volume element dV and the surface area element dA in the volume and surface integrals in Eq. (A.1) include a factor of $2\pi r$ for integration in cylindrical coordinates (r, z), to account for the axisymmetric formulation.

A.2. Weak formulation for the P&W scheme

In order to prescribe the crack width as the boundary condition in the tip region Σ_t, the *P&W* scheme employs the localized mixed hybrid formulation from Zilian and Fries (2009) for finite elements that overlap with the crack tip region Σ_t. In finite elements overlapping with the tip region Σ_t, the stress $\boldsymbol{\sigma}$ is introduced as an auxiliary tensor variable for which Hooke's law (3) is weakly imposed. The formulation for the rest of the domain is similar to the $P \to W$ scheme.
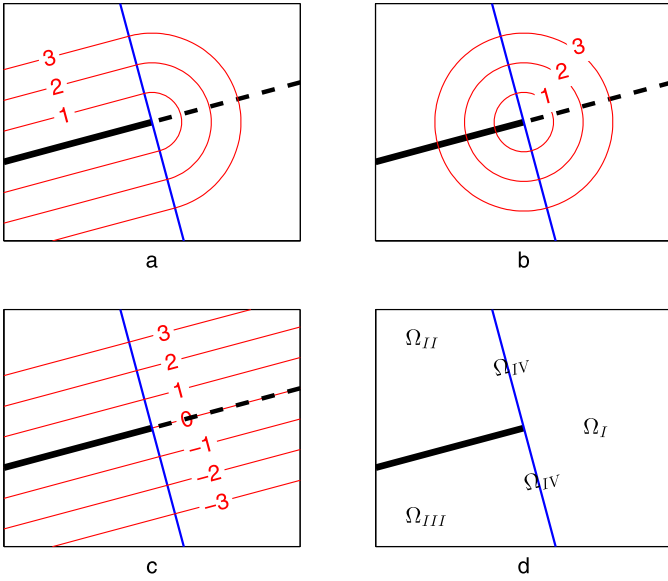
Fig. A.19. Isolines for level-set functions (a) $\phi_1(\boldsymbol{x}) = 1, 2, 3$, (b) $\phi_2(\boldsymbol{x}) = 1, 2, 3$, and (c) $\phi_3(\boldsymbol{x}) = -3, -2, -1, 0, 1, 2, 3$, and (d) the sets Ω_I, Ω_{II}, Ω_{III}, Ω_{IV} defined by the level-set functions for a 2D crack description. Solid black lines denote the crack Σ; dashed black lines denote the extended crack $\hat{\Sigma}$; blue lines denote the set Ω_{IV} (the boundary of the set Ω_I); red lines denote the isolines of the level-set functions. (For interpretation of the references to color in this figure legend, the reader is referred to the web version of this article.)

The weak formulation for the *P&W* scheme for a plane strain fracture in an infinite domain was given in Eqs. (41)–(43) in Gordeliy and Peirce (2013b). Modifications for an axisymmetric fracture are introduced in the same way as in Eq. (A.1) for the $P \rightarrow W$ scheme, by replacing the arc-length element dζ in the integrals over the crack surface in Eqs. (41)–(43) in Gordeliy and Peirce (2013b) by the surface area element dA, including the $2\pi r$ factor for integration in cylindrical coordinates (r, z) in the volume element dV and the surface area element dA in the volume and surface integrals, and rewriting the elastic tensors and tensor operations in the cylindrical coordinates (r, z). If the problem under consideration includes prescribed surface tractions t_i^* over a part of the domain boundary $\Gamma_{t, i}$, the weak formulation includes the corresponding integral over the boundary $\Gamma_{t, i}$ as in Eq. (A.1).

A.3. Level-set representation of the fracture

The crack is represented by the following three level-set functions (Fries and Baydoun, 2012):

- $\phi_1(\boldsymbol{x}) = \min_{\tilde{\boldsymbol{x}} \in \Sigma} |\boldsymbol{x} - \tilde{\boldsymbol{x}}|$ is the distance to the crack Σ (or to the virtual crack extension Σ, for the XFEM-s scheme);
- $\phi_2(\boldsymbol{x}) = |\boldsymbol{x} - \boldsymbol{x}_{tip}|$ is the distance to the crack tip $\boldsymbol{x}_{tip}$;
- $\phi_3(\boldsymbol{x}) = \pm\min_{\hat{\boldsymbol{x}} \in \hat{\Sigma}} |\boldsymbol{x} - \hat{\boldsymbol{x}}|$ is the signed distance to the extended crack $\hat{\Sigma}$. The extended crack $\hat{\Sigma}$ includes the crack Σ (and the virtually extended crack Σ, for the XFEM-s scheme) and extends beyond each crack tip in the direction tangent to the crack to infinity. The sign of $\phi_3(\boldsymbol{x})$ is defined by the direction of the normal vector of the crack segment that contains the nearest point to $\boldsymbol{x}$. Note that we thus define two crack extensions: the virtually extended crack Σ, for the XFEM-s scheme, extends to the boundaries of the crack-tip finite elements; the extended crack $\hat{\Sigma}$ extends to infinity.

The isolines for the level-set functions ϕ_j ($j = 1, 2, 3$) are shown in Fig. A.19. Whereas in 2D, two level-set functions would be sufficient to define a crack (e.g., as in Stolarska et al., 2001),

the present representation by the three level-set functions can be extended to 3D cracks in a straightforward manner (Fries and Baydoun, 2012). In the numerical implementation, the level-set functions ϕ_j ($j = 1, 2, 3$) are employed to determine which nodes of the mesh are to be enriched with either sign or crack-tip enrichments (Fries and Baydoun, 2012), and to define the curvilinear polar coordinates, $(\rho(\boldsymbol{x}), \theta(\boldsymbol{x}))$, associated with the crack and employed in Eq. (26) to calculate the crack-tip enrichment functions.

For computational efficiency, the level-set functions ϕ_j ($j = 1, 2, 3$) are computed at the nodes of the FEM mesh and are interpolated in the domain using the Lagrange shape functions, via

$$\phi_j^h(\boldsymbol{x}) = \sum_{i \in I} \phi_j(\boldsymbol{x}_i) N_i(\boldsymbol{x}) \tag{A.2}$$

This discretization of the level-set functions translates into an approximate representation of the crack surface (Fries and Baydoun, 2012).

The polar coordinates $(\rho(\boldsymbol{x}), \theta(\boldsymbol{x}))$, used to evaluate the crack-tip enrichment functions (26) for any point $\boldsymbol{x}$ in the domain, are defined as follows. The domain is decomposed into four sets, Ω_I, Ω_{II}, Ω_{III}, Ω_{IV}, shown in Fig. A.19 and defined by:

$$\Omega_I = \{\boldsymbol{x} : \phi_1 \neq |\phi_3|\} \tag{A.3}$$

$$\Omega_{II} = \{\boldsymbol{x} : \phi_1 < \phi_2, \phi_3 > 0\} \tag{A.4}$$

$$\Omega_{III} = \{\boldsymbol{x} : \phi_1 < \phi_2, \phi_3 \leq 0\} \tag{A.5}$$

$$\Omega_{IV} = \{\boldsymbol{x} : \phi_1 = \phi_2 = |\phi_3|\} \tag{A.6}$$

In addition, an auxiliary angle $\theta^*(\boldsymbol{x})$ is defined by

$$\theta^*(\boldsymbol{x}) = \sin^{-1} \frac{\phi_3(\boldsymbol{x})}{\phi_2(\boldsymbol{x})} \tag{A.7}$$

The polar coordinates $(\rho(\boldsymbol{x}), \theta(\boldsymbol{x}))$ for a point $\boldsymbol{x}$ are then defined by

$$\rho(\boldsymbol{x}) = \phi_2(\boldsymbol{x}) \tag{A.8}$$

$$\theta(\boldsymbol{x}) = \begin{cases} \theta^*(\boldsymbol{x}), & \boldsymbol{x} \in \Omega_I \\ \pi - \theta^*(\boldsymbol{x}), & \boldsymbol{x} \in \Omega_{II} \\ -\pi - \theta^*(\boldsymbol{x}), & \boldsymbol{x} \in \Omega_{III} \\ \theta^*(\boldsymbol{x}) = \pm\frac{\pi}{2}, & \boldsymbol{x} \in \Omega_{IV} \end{cases} \tag{A.9}$$

The following comments must be made about the definition of the sets Ω_I, Ω_{II}, Ω_{III}, Ω_{IV} in the present work:

- In the present paper, axisymmetric cracks are represented by 1D curves in a 2D domain. We assume that the crack is extended in the direction tangential to the crack, as shown in Fig. A.19. In this case, the set Ω_{IV} is a straight line orthogonal to the crack and intersecting the crack at the crack tip (Fig. A.19). In the work of Fries and Baydoun (2012), a more general 3D crack description is discussed. In Fig. 11 in Fries and Baydoun (2012), the crack extension is not tangential to the crack, and the set Ω_{IV} is a region (not a line). However, it is mentioned in Fries and Baydoun (2012) that for a 2D crack description, the crack can be extended along the crack direction.
- We have used alternative definitions (A.4) and (A.5) of the sets Ω_{II} and Ω_{III} to those in Fries and Baydoun (2012), due to the sensitivity of the regions Ω_{II} and Ω_{III} defined in Fries and Baydoun (2012) to slight numerical errors in the values of ϕ_1 and ϕ_3.

Appendix B. Approximations of pressure and influence matrix

B.1. Hydraulic fracture with fluid lag, P → W scheme

The fluid pressure $p_f(s, t)$ is expanded in terms of the basis functions $h_{i+1/2}(s)$ associated with the nodal values $p_{i+1/2} = p_f(s_{i+1/2}, t)$, as shown by Eq. (30). The piecewise linear basis functions $h_{i+1/2}(s)$, associated with the nodes $s_{i+1/2}$, are defined as

$$h_{i+1/2}(s) = \begin{cases} \dfrac{s - s_{i-1/2}}{s_{i+1/2} - s_{i-1/2}}, & \text{if } s_{i-1/2} \leq s < s_{i+1/2} \\ \dfrac{s_{i+3/2} - s}{s_{i+3/2} - s_{i+1/2}}, & \text{if } s_{i+1/2} \leq s < s_{i+3/2}, \ i = 2, \dots, m \\ 0, & \text{else} \end{cases} \quad \text{(B.1)}$$

$$h_{3/2}(s) = \begin{cases} 1, & \text{if } s < s_{3/2} \\ \dfrac{s_{5/2} - s}{s_{5/2} - s_{3/2}}, & \text{if } s_{3/2} \leq s < s_{5/2} \\ 0, & \text{else} \end{cases} \quad \text{(B.2)}$$

$$h_{m+3/2}(s) = \begin{cases} \dfrac{s - s_{m+1/2}}{s_{m+3/2} - s_{m+1/2}}, & \text{if } s_{m+1/2} \leq s \leq \ell_f \\ 0, & \text{else} \end{cases} \quad \text{(B.3)}$$

We consider a finite domain V with prescribed tractions on the external boundaries $\Gamma_{t,i}$ and with zero displacement u_i on the external boundaries $\Gamma_{u,i}$ for $i = 1, 2$. (More general cases with infinite boundaries and/or applied nonzero displacements can be treated via straightforward modifications.) Due to the linearity of the elasticity problem, the crack width $w(s, t)$ can be found as the superposition of the following basis functions:

$$w(s, t) \approx \sum_{j=1}^{m+1} p_{j+1/2} \omega_{j+1/2}(s) + \omega_\sigma(s) \quad \text{(B.4)}$$

where

- $\omega_{j+1/2}(s)$ for $j = 1, \dots, m + 1$ represents the jump in the normal displacement across Σ that is the XFEM solution to the boundary value problem in which the prescribed pressure in the crack is given by the basis function $h_{j+1/2}(s)$, and any loads, applied to the external boundaries of the domain V, are set to zero:

$$\sigma_n^+ = \sigma_n^- = -h_{j+1/2}(s) \quad \text{for } s \in \Sigma, \quad \sigma_s^+ = \sigma_s^- = 0$$
$$\text{for } s \in \Sigma; \quad t_i = 0 \quad \text{on } \Gamma_{t,i}, \ i = 1, 2 \quad \text{(B.5)}$$

- $\omega_\sigma(s)$ represents the jump in the normal displacement across Σ that is the XFEM solution to the boundary value problem with zero pressure in the crack and any tractions, applied to the external boundaries $\Gamma_{t,i}$, set to their values t_i^* in the original problem:

$$\sigma_n^+ = \sigma_n^- = 0 \quad \text{for } s \in \Sigma, \quad \sigma_s^+ = \sigma_s^- = 0$$
$$\text{for } s \in \Sigma; \quad t_i = t_i^* \quad \text{on } \Gamma_{t,i}, \ i = 1, 2 \quad \text{(B.6)}$$

Evaluating the width basis functions $\omega_{j+1/2}(s)$ and $\omega_\sigma(s)$ at nodes s_i, $i = 1 : N$, we obtain the influence matrix $D_{ij} = \omega_{j+1/2}(s_i)$ and the effect of tractions applied to the external boundaries $\omega_{\sigma,i} = \omega_\sigma(s_i)$. Then the XFEM approximation for the nodal crack widths can be written in the form of Eq. (31).

B.2. Hydraulic fracture without fluid lag, P&W scheme

We consider an infinite domain V with applied far-field stresses σ_{ij}^∞, for the P&W scheme. (More general cases of boundary conditions for a finite or an infinite domain can be treated via straightforward modifications.) The crack width $w(s, t)$ in the channel can be approximated as the superposition of the following width basis functions:

$$w(s, t) \approx \sum_{j=1}^{m+1} p_{j+1/2} \omega_{j+1/2}(s) + \omega_t(s) + \omega_\sigma(s), \quad s \in \Sigma_c \quad \text{(B.7)}$$

where the width basis functions represent the jump in the normal displacement across Σ that are the XFEM solutions to the following mixed boundary value problems:

- $\omega_{j+1/2}(s)$ for $j = 1, \dots, m + 1$ is the XFEM solution to the problem in which the prescribed pressure in the channel is given by the basis function $h_{j+1/2}(s)$ while the crack width in the tip region is set to zero:

$$\sigma_n^+ = \sigma_n^- = -h_{j+1/2}(s) \quad \text{for } s \in \Sigma_c, \quad \sigma_s^+ = \sigma_s^- = 0 \quad \text{for } s \in \Sigma \quad \text{(B.8)}$$

$$w(s) = [[\mathbf{u}]]_\Sigma \cdot \mathbf{n} = 0 \quad \text{for } s \in \Sigma_t \quad \text{(B.9)}$$

- $\omega_t(s)$ is the XFEM solution to the problem with zero pressure in the channel, and the crack width in the tip region set to the tip asymptote,

$$\sigma_n^+ = \sigma_n^- = 0 \quad \text{for } s \in \Sigma_c, \quad \sigma_s^+ = \sigma_s^- = 0 \quad \text{for } s \in \Sigma \quad \text{(B.10)}$$

$$w(s) = [[\mathbf{u}]]_\Sigma \cdot \mathbf{n} = w_{tip}(s) \quad \text{for } s \in \Sigma_t \quad \text{(B.11)}$$

- $\omega_\sigma(s)$ is the XFEM solution to the problem with the normal traction in the channel and the shear traction in the crack given by the tractions corresponding to the far-field stress, according to Eqs. (8) and (10):

$$\sigma_n^+ = \sigma_n^- = \sigma_n^\infty \quad \text{for } s \in \Sigma_c, \quad \sigma_s^+ = \sigma_s^- = \sigma_s^\infty \quad \text{for } s \in \Sigma \quad \text{(B.12)}$$

and for which the crack width in the tip region is set to zero as in Eq. (B.9).

All width basis functions are obtained by using the P&W XFEM scheme. The crack width constraints (B.9) and (B.11) are set via the weak formulation.

Evaluating the width basis functions $\omega_{j+1/2}(s)$, $\omega_t(s)$ and $\omega_\sigma(s)$ at nodes s_i, $i = 1 : N$, we obtain the influence matrix $D_{ij} = \omega_{j+1/2}(s_i)$, the effect of crack-tip width $\omega_{t,i} = \omega_t(s_i)$, and the effect of the far-field stress $\omega_{\sigma,i} = \omega_\sigma(s_i)$. Then the XFEM approximation for the nodal crack widths can be written in the form of Eq. (44).

Appendix C. Scaling for numerical computations

The problem of hydraulic fracture propagation involves quantities at multiple scales that differ by several orders of magnitude, e.g., a crack width in the order of 10^{-4} m, a fracture radius of order 10^{-1} m in the laboratory and tens of meters in the field, stresses of order of 10^6 Pa, Young's modulus of order 10^{10} Pa, etc. Combinations of such quantities in a numerical scheme can reduce the overall accuracy of the solution due to machine precision issues. To improve the accuracy of numerical solutions, we introduce characteristic scales for the unknowns in the problem to numerically handle quantities of orders 10^{-1}–10^2. Thus, for the numerical computations, we scale all the governing equations and the

equations for the XFEM algorithm (i.e., Eqs. (2)–(52)) using the following characteristic scales for time (t_*), length (ℓ_*), pressure (p_*), crack width (w_*), and fluid flow rate (Q_*) (scaling formulation from Bunger et al., 2013):

$$t_* = \left(\frac{\mu' \ell_*^9}{E' Q_*^3}\right)^{1/4}, \quad p_* = \left(\frac{\mu' Q_* E'^3}{\ell_*^3}\right)^{1/4}, \quad w_* = \left(\frac{\mu' Q_* \ell_*}{E'}\right)^{1/4}$$

$$\text{(C.1)}$$

$$t = t_* \tilde{t}, \quad s = \ell_* \tilde{s}, \quad \ell(t) = \ell_* \tilde{\ell}(\tilde{t}), \quad \ell_f(t) = \ell_* \tilde{\ell}_f(\tilde{t}) \tag{C.2}$$

$$r = \ell_* \tilde{r}, \quad R(t) = \ell_* \tilde{R}(\tilde{t}), \quad R_f(t) = \ell_* \tilde{R}_f(\tilde{t}) \tag{C.3}$$

$$p_f(s, t) = p_* \tilde{p}_f(\tilde{s}, \tilde{t}), \quad \sigma_{ij} = p_* \tilde{\sigma}_{ij} \tag{C.4}$$

$$w(s, t) = w_* \tilde{w}(\tilde{s}, \tilde{t}), \quad u_i = w_* \tilde{u}_i \tag{C.5}$$

$$q(s, t) = Q_* \tilde{q}(\tilde{s}, \tilde{t}), \quad Q(t) = Q_* \tilde{Q}(\tilde{t}) \tag{C.6}$$

where the resulting dimensionless quantities are time $\tilde{t}$, arc-length coordinate $\tilde{s}$, crack length $\tilde{\ell}$, fluid front $\tilde{\ell}_f$, radial coordinate $\tilde{r}$, fracture radius $\tilde{R}$, fluid front radius $\tilde{R}_f$, fluid pressure $\tilde{p}_f$, stress field $\tilde{\sigma}_{ij}$, crack width $\tilde{w}$, displacement field $\tilde{u}_i$, fluid flux $\tilde{q}$, and fluid injection rate $\tilde{Q}$. The characteristic scales are used to pre-condition the input data to the XFEM-ILSA model (such as the Young's modulus E, fluid viscosity μ, fracture toughness K_{Ic}, injection rate $Q(t)$, length dimensions of the domain and of the initial crack, applied boundary tractions, far-field stress, etc.) and to scale the output of the numerical model back to the physical dimensions. The resulting equations for the dimensionless quantities ($\tilde{t}, \tilde{s}, \tilde{\ell}, \tilde{\ell}_f, \tilde{r}, \tilde{R}, \tilde{R}_f, \tilde{p}_f, \tilde{\sigma}_{ij}, \tilde{w}, \tilde{u}_i, \tilde{q}, \tilde{Q}$) can be obtained from the equations for the corresponding physical quantities ($t, s, \ell, \ell_f, r, R, R_f p_f, \sigma_{ij}, w, u_i, q, Q$), upon the change of quantities from physical to dimensionless, $\{t, s, \ell, \ell_f, r, R, R_f p_f, \sigma_{ij}, w, u_i, q, Q\} \mapsto$

$\{\tilde{t}, \tilde{s}, \tilde{\ell}, \tilde{\ell}_f, \tilde{r}, \tilde{R}, \tilde{R}_f, \tilde{p}_f, \tilde{\sigma}_{ij}, \tilde{w}, \tilde{u}_i, \tilde{q}, \tilde{Q}\}$, and the change of the material properties from physical to scaled, $\{K', E', \mu'\} \mapsto \{\tilde{K}', \tilde{E}', \tilde{\mu}'\}$, where

$$\tilde{K}' = \frac{K'}{(Q_* E'^3 \mu' \ell_*^{-1})^{1/4}}, \quad \tilde{E}' = 1, \quad \tilde{\mu}' = 1 \tag{C.7}$$

The characteristic length-scale ℓ_* in (C.1) is chosen according to the expected scale of the fracture radius, e.g., $\ell_* = 10^{-3}$ m for the simulations of laboratory experiments described in Section 5. The characteristic fluid flux scale Q_* in (C.1) can be chosen, e.g., as $Q_* = Q(t_1)$ where t_1 is the initial time of the simulation.

Appendix D. XFEM solution for a fracture in the vicinity of a finite-element node

In the XFEM solution, we assume that the crack does not cut through the nodes of the finite element mesh. This assumption does not limit the applicability of the present XFEM to modeling an arbitrary crack path. If a crack extension segment is predicted to pass through a node of the finite-element mesh, a negligibly small perturbation is introduced to the direction of the crack extension so that the crack does not pass through the finite-element (FE) node but passes its vicinity.

We have not observed any issues in the present model when the crack passes the vicinity of a FE node. As an example, we consider the solution obtained at time $t = 4.7$ s in the XFEM simulation for the laboratory test *pg1*, described in Section 5.2.6. Fig. D.20 shows the computed fracture path in the background finite-element mesh. Several locations are observed where the fracture passes in a close proximity to a FE node. At $r = 11.78$ mm, the fracture passes within a distance of the order 10^{-9} mm from the closest FE node, and the length of the crack element $[s_i, s_{i+1}]$ created between the two intersections of the fracture with the FE edges adjacent to this FE node, is of the order 10^{-9} mm. One cannot distinguish between these two crack nodes in Fig. D.20. However, the solution for the crack width and the fluid pressure, obtained from the coupled XFEM-HF model, is smooth around $r = 11.78$ mm and does not show any issue (Fig. D.21).
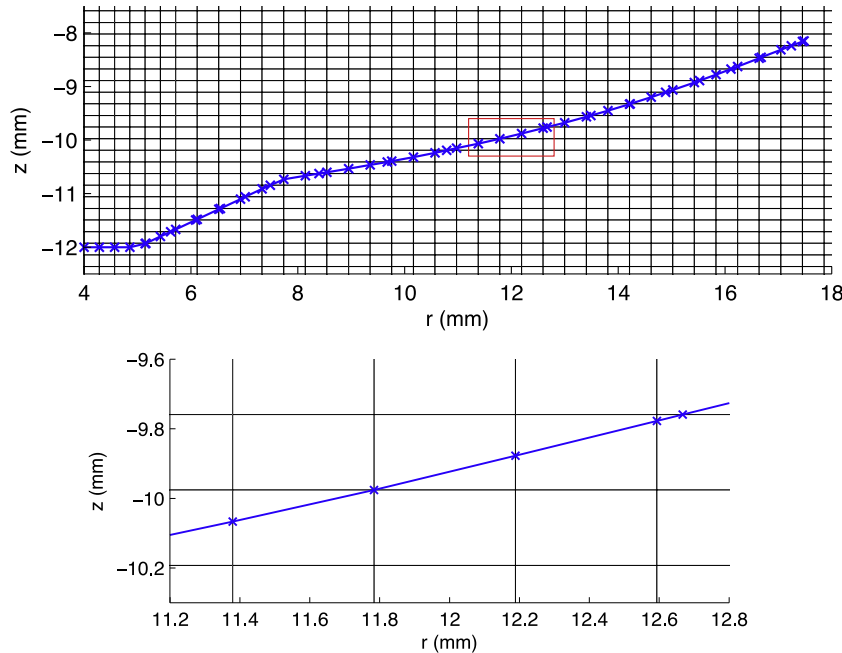
Fig. D.20. Computed fracture path for test *pg1* and the background finite-element mesh, with an inset area marked by a red line (top), and mesh detail in the inset area (bottom). The fracture path is shown by the blue line; the cross markers depict locations of crack-width nodes. (For interpretation of the references to color in this figure legend, the reader is referred to the web version of this article.)
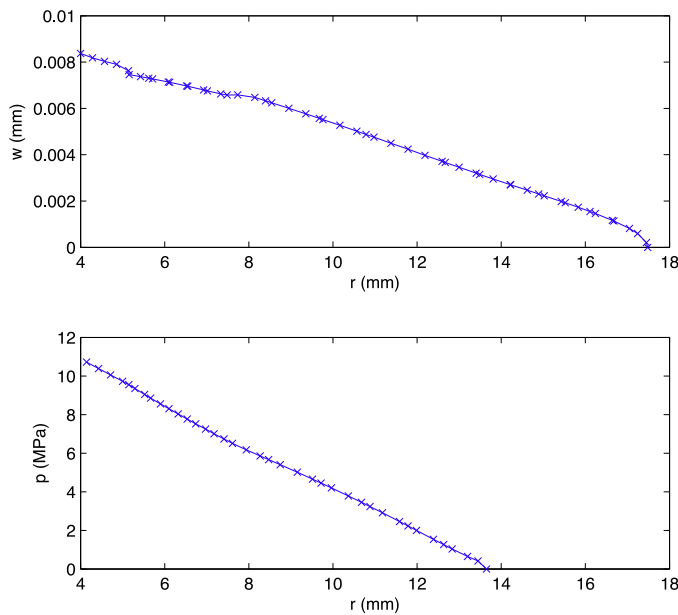
Fig. D.21. Crack width and fluid pressure at time $t = 4.7$ s, computed in the XFEM simulation for test *pg1*.

References

Abbas, S., Gordeliy, E., Peirce, A., 2016. Modeling multiple curved fractures connected through a wellbore using a fluid-coupled XFEM algorithm. ARMA, Houston.

Baydoun, M., Fries, T.-P., 2012. Crack propagation criteria in three dimensions using the xfem and an explicit-implicit crack description. Int. J. Fract. 178, 51–70.

Bettess, P., 1992. Infinite Elements. Penshaw Press.

Bunger, A., 2005. Near-Surface Hydraulic Fracture. University of Minnesota, Ph.D. thesis.

Bunger, A., Jeffrey, R., Detournay, E., 2004. Toughness-dominated near-surface hydraulic fracture experiments. In: Yale, D.P., Willson, S.M., Abou-Sayed, A.S. (Eds.), GulfRock04 Conference. ARMA, Houston.

Bunger, A.P., Gordeliy, E., Detournay, E., 2013. Comparison between laboratory experiments and coupled simulations of saucer-shaped hydraulic fractures in homogeneous brittle-elastic solids. J. Mech. Phys. Solids 61 (7), 1636–1654.

Castonguay, S.T., Mear, M.E., Dean, R.H., Schmidt, J.H., 2013. Predictions of the growth of multiple interacting hydraulic fractures in three dimensions. Soc. Petrol. Eng., New Orleans. SPE 166259

Cherny, S., Lapin, V., Esipov, D., Kuranakov, D., Avdyushenko, A., Lyutov, A., Karnakov, P., 2016. Simulating fully 3D non-planar evolution of hydraulic fractures. Int. J. Fract. 201 (2), 181–211.

Damjanac, B., Detournay, C., Cundall, P., Varun, 2013. Three-Dimensional Numerical Model of Hydraulic Fracturing in Fractured Rock Masses. InTech.

Desroches, J., Detournay, E., Lenoach, B., Papanastasiou, P., Pearson, J., Thiercelin, M., Cheng, A.-D., 1994. The crack tip region in hydraulic fracturing. Proc. Roy. Soc. Lond. Ser. A 447, 39–48.

Detournay, E., Peirce, A., 2014. On the moving boundary conditions for a hydraulic fracture. Int. J. Eng. Sci. 84, 147–155.

Dontsov, E., Peirce, A., 2015. A non-singular integral equation formulation to analyse multiscale behaviour in semi-infinite hydraulic fractures. J. Fluid Mech. 781, R1.

Erdogan, F., Sih, G.C., 1963. On the crack extension in plates under plate loading and transverse shear. J. Basic Eng. 85, 519–527.

Faivre, M., Paul, B., Golfier, F., Giot, R., Massin, P., Colombo, D., 2016. 2D coupled HM-XFEM modeling with cohesive zone model and applications to fluid-driven fracture network. Eng. Fract. Mech. 159, 115–143.

Fata, S.N., 2016. Coupling elasticity and fluid flow for a 3D hydraulic fracturing solver. ARMA, Houston.

Fries, T.-P., 2008. A corrected XFEM approximation without problems in blending element. Int. J. Numer. Meth. Eng. 75, 503–532.

Fries, T.-P., Baydoun, M., 2012. Crack propagation with the extended finite element method and a hybrid explicit-implicit crack description. Int. J. Numer. Meth. Eng. 89, 1527–1558.

Fries, T.-P., Belytschko, T., 2010. The extended/generalized finite element method: an overview of the method and its applications. Int. J. Numer. Meth. Eng. 84, 253–304.

Gao, H., Rice, J., 1985. Somewhat circular tensile cracks. Int. J. Fract. 33, 155–174.

Garagash, D., Detournay, E., 2000. The tip region of a fluid-driven fracture in an elastic medium. ASME J. Appl. Mech. 67 (1), 183–192.

Garagash, D., Detournay, E., Adachi, J., 2011. Multiscale tip asymptotics in hydraulic fracture with leak-off. J. Fluid Mech. 669, 260–297.

Gordeliy, E., Detournay, E., 2011. Displacement discontinuity method for modeling axisymmetric cracks in an elastic half-space. Int. J. Solids Struct. 48, 2614–2629.

Gordeliy, E., Peirce, A., 2013a. Coupling schemes for modeling hydraulic fracture propagation using the XFEM. Comput. Methods Appl. Mech. Eng. 253, 305–322.

Gordeliy, E., Peirce, A.P., 2013b. Implicit level set schemes for modeling hydraulic fractures using the XFEM. Comput. Methods Appl. Mech. Eng. 266, 125–143.

Gordeliy, E., Peirce, A.P., 2015. Enrichment strategies and convergence properties of the XFEM for hydraulic fracture problems. Comput. Methods Appl. Mech. Eng. 283, 474–502.

Gosz, M., Moran, B., 2002. An interaction energy integral method for computation of mixed-mode stress intensity factors along non-planar crack fronts in three dimensions. Eng. Fract. Mech. 69, 299–319.

Gupta, P., Duarte, C.A., 2016. Coupled formulation and algorithms for the simulation of non-planar three-dimensional hydraulic fractures using the generalized finite element method. Int. J. Numer. Anal. Meth. Geomech. 40, 1402–1437.

Haddad, M., Sepehrnoori, K., 2016. XFEM-based CZM for the simulation of 3D multiple-cluster hydraulic fracturing in quasi-brittle shale formations. Rock Mech. Rock Eng. 49, 4731–4748. doi:10.1007/s00603-016-1057-2.

Kumar, D., Ghassemi, A., 2016. A three-dimensional analysis of simultaneous and sequential fracturing of horizontal wells. J. Petrol. Sci. Eng. 146, 1006–1025.

Lecampion, B., 2009. An extended finite element method for hydraulic fracture problems. Commun. Numer. Meth. Eng. 25, 121–133.

Lecampion, B., Bunger, A., Zhang, X., 2018. Numerical methods for hydraulic fracture propagation: a review of recent trends. J. Nat. Gas Sci. Eng. 49, 66–83.

Liu, G.R., Quek, S.S., 2003. The Finite Element Method: A Practical Course. Elsevier Science Ltd., Butterworth-Heinemann.

Marques, J., Owen, D., 1984. Infinite elements in quasi-static materially nonlinear problems. Comput. Struct. 18 (4), 739–751.

Moës, N., Dolbow, J., Belytschko, T., 1999. A finite element method for crack growth without remeshing. Int. J. Numer. Meth. Eng. 46, 131–150.

Peirce, A., 2016. Implicit level set algorithms for modelling hydraulic fracture propagation. Phil. Trans. R. Soc. A 374, 20150423. doi:10.1098/rsta.2015.0423.

Peirce, A.P., Detournay, E., 2008. An implicit level set method for modeling hydraulically driven fractures. Comput. Meth. Appl. Mech. Eng. 197, 2858–2885. doi:10.1016/j.cma.2008.01.013.

Rice, J., 1968. Mathematical analysis in the mechanics of fracture. In: Liebowitz, H. (Ed.), Fracture, an Advanced Treatise. Academic Press, New York NY. II. 3, 191–311

Rice, J.R., 1968. A path independent integral and the approximate analysis of strain concentration by notches and cracks. J. Appl. Mech. 35, 379–386.

Savitski, A., Detournay, E., 2002. Propagation of a fluid-driven penny-shaped fracture in an impermeable rock: asymptotic solutions. Int. J. Solids Struct. 39 (26), 6311–6337.

Searles, K.H., Zielonka, M.G., Ning, J., Garzon, J.L., Kostov, N.M., Sanz, P.F., Biediger, E., 2016. Fully-coupled 3D hydraulic fracture models: Development, validation, and application to O&G problems. Society of Petroleum Engineers, The Woodlands. SPE 179121-MS

Settgast, R.R., Fu, P., Walsh, S.D.C., White, J.A., Annavarapu, C., Ryerson, F.J., 2017. A fully coupled method for massively parallel simulation of hydraulically driven fractures in 3-dimensions. Int. J. Numer. Anal. Meth. Geomech. 41, 627–653.

Sherman, C., Aarons, L., Morris, J., Johnson, S., Savitski, A., Geilikman, M., 2015. Finite Element Modeling of Curving Hydraulic Fractures and Nearwellbore Hydraulic Fracture Complexity. ARMA, San Francisco.

Stolarska, M., Chopp, D., Moes, N., Belytschko, T., 2001. Modeling crack growth by level sets and the extended finite element method. Int. J. Numer. Meth. Eng. 51, 943–960.

Sukumar, N., Prevost, J.-H., 2003. Modeling quasi-static crack growth with the extended finite element method Part I: Computer implementation. Int. J. Solids Struct. 40, 7513–7537.

Weber, N., Siebert, P., Willbrand, K., Feinendegen, M., Clauser, C., Fries, T.P., 2013. The XFEM With an Explicit-Implicit Crack Description for Hydraulic Fracture Problems. InTech.

Wong, S., Geilikman, M., Xu, G., 2013. The geomechanical interaction of multiple hydraulic fractures in horizontal wells. InTech.

Zhang, F., Mack, M., 2016. Modeling of Hydraulic Fracture Initiation from Perforation Tunnels Using the 3D Lattice Method. ARMA, Houston.

Zhang, X., Detournay, E., Jeffrey, R., 2002. Propagation of a penny-shaped hydraulic fracture parallel to the free-surface on an elastic half-space. Int. J. Fract. 115, 125–158.

Zielonka, M.G., Searles, K.H., Ning, J., Buechler, S.R., 2014. Development and validation of fully-coupled hydraulic fracturing simulation capabilities. Proceedings of 2014 SIMULIA Community Conference, Providence, RI.

Zienkiewicz, O.C., Emson, C.R.I., Bettess, P., 1983. A novel boundary infinite element. Int. J. Num. Meth. Eng. 19, 393–404.

Zienkiewicz, O.C., Taylor, R.L., Zhu, J.Z., 2013. The Finite Element Method: its Basis and Fundamentals, 7th ed. Elsevier.

Zilian, A., Fries, T.-P., 2009. A localized mixed-hybrid method for imposing interfacial constraints in the extended finite element method (XFEM). Int. J. Numer. Meth. Eng. 79, 733–752.